

AD-A098 123

NAVAL RESEARCH LAB WASHINGTON DC

F/G 20/9

A FULLY TWO-DIMENSIONAL EQUILIBRIUM AND TRANSPORT MODEL OF THE --ETC(U)

APR 81 M H EMERY, N K WINSOR

UNCLASSIFIED NRL-MR-4498

NL

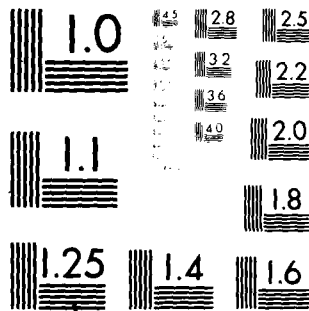
END

DATE

FILED

13-81

DTIC



MICROCOPY RESOLUTION TEST CHART  
NATIONAL BUREAU OF STANDARDS-1963-A

1990

SECURITY CLASSIFICATION OF THIS PAGE (When Data Entered)

DD FORM 1 JAN 73 1473

EDITION OF 1 NOV 68 IS OBSOLETE  
S/N 0102-014-6601

**SECURITY CLASSIFICATION OF THIS PAGE (When Data Entered)**

20. ABSTRACT (Continued)

We present here the methods we have developed to calculate equilibria and transport in a fully two-dimensional geometry. The model is sufficiently general that it is capable of calculating equilibria and transport given rather general plasma geometries and coil structures. Here we apply the model to the poloidal divertor system and describe the results.

ACCESSION

FILE

DATE

BY

REMARKS

A

# CONTENTS

I.	INTRODUCTION.....	1
II.	PHYSICAL MODEL.....	7
	A. Transport.....	7
	B. Coordinate System.....	11
	C. Currents.....	13
	D. Electric Fields.....	15
	E. Velocities.....	18
III.	COMPUTATIONAL MODEL.....	20
	A. Introduction.....	20
	B. Currents.....	23
	C. Electric Fields.....	25
	D. Velocities.....	25
	E. Mass and Energy Transport.....	26
	F. Exactness of Conservation Equations.....	30
IV.	SIMPLIFIED MODEL.....	35
	A. Time Scales.....	35
	B. Perpendicular Transport.....	37
	C. Simplified Transport Equations.....	37
V.	ANALYTIC BENCHMARK.....	39
	A. Ordering.....	39
	B. First-Order Equations.....	41
VI.	NUMERICAL RESULTS.....	45
	A. Equilibrium.....	45
	B. Transport.....	48
VII.	SUMMARY AND CONCLUSIONS.....	52
	ACKNOWLEDGMENTS.....	54
	APPENDIX.....	55
	REFERENCES.....	58

## A FULLY TWO-DIMENSIONAL EQUILIBRIUM AND TRANSPORT MODEL OF THE POLOIDAL DIVERTOR

### I. INTRODUCTION

Tokamak designs are becoming very complex. In order to improve the confinement time and increase the beta, present and future-generation toroidal confinement devices may have non-circular cross-sections or multiple magnetic axes or both. Vertically elongated cross-sections promise improved stability coupled with higher values of the plasma current and total beta.<sup>1</sup> There are indications that substantially higher plasma pressures can be more confined in doublet geometries than in circular geometries.<sup>2</sup> To control the level of impurities and thus increase confinement time, a divertor will be needed in tokamak reactors.<sup>3</sup> These essential features of research devices demonstrate the need for a multidimensional model to investigate equilibrium and transport in present and proposed experiments. The simple low-beta, one-dimensional, circular flux surface model is not adequate to describe the physics of these sophisticated devices.

In an elongated or "D" shaped discharge, the curvature varies greatly and the transport coefficients cannot be approximated by surface averaged quantities, as in the usual one-dimensional schemes. In a high beta discharge, the flux surfaces change shape as a function of time and a multi-dimensional scheme is required to model this

Manuscript submitted February 17, 1981.

effect. The doublet and poloidal divertor systems contain multiple magnetic axes with a separatrix. They are inherently two-dimensional.

We present here the methods we have developed to calculate equilibria and transport in a fully two-dimensional geometry. The model is sufficiently general that it is capable of calculating equilibria and transport given rather general plasma geometries and coil structures. Here we apply the model to the poloidal divertor system (the Princeton Poloidal Divertor Experiment (PDX)<sup>4</sup>) and describe the results.

We have developed a fully two-dimensional Eulerian-Lagrangian computer simulation model of tokamak discharges. This computer model is used to investigate the time evolution of a finite-conductivity plasma in a finite-conductivity vessel. It uses as a finite-difference mesh a general-connectivity triangular grid. This permits the investigation of problems of much greater complexity than more conventional one- or two-dimensional schemes. This code is an extension of the previously reported circular tokamak models<sup>5,6</sup> which were an outgrowth of the Linus projects.<sup>7</sup>

The code we have developed is designed to follow simultaneously the resistive diffusion, transport and gross dynamics of a magnetically confined plasma of arbitrary shape. The finite resistivity of the confining shell permits us to examine the discharge for times exceeding the penetration time of the magnetic fields through the copper shell. The model is based on the quasi-static evolution of force balance in the plasma.

The simplest set of equations which describe a plasma in equilibrium with a magnetic field is



$$\nabla p = \frac{1}{c} \underline{j} \times \underline{B}, \quad (\text{I-1})$$

$$\nabla \times \underline{B} = \frac{4\pi}{c} \underline{j}, \quad (\text{I-2})$$

$$\nabla \cdot \underline{B} = 0. \quad (\text{I-3})$$

Eq. I-1 stems from the equation of motion. The force balance between the plasma pressure and magnetic forces accurately represents a system that evolves in time, provided the evolution is slow and nonideal forces are weak. Generally, this implies that the system changes on a time scale characterized by the resistive diffusion time. The question of time scales is treated in more detail in Section IV.

The usual method for determining this equilibrium consists of casting Eqs. (I-1) - (I-2) into the form of a nonlinear, elliptic, partial differential equation for the flux function  $\psi$ .<sup>8</sup> This resulting equation is then differenced on an Eulerian mesh and solved by iteration subject to appropriate boundary conditions.

Our method for calculating the equilibrium is quite different. The equilibrium equations describe the relations between nested toroidal surfaces<sup>9</sup> (flux surfaces). The plasma pressure is constant on these surfaces and  $\underline{B}$  and  $\underline{j}$  lie on these surfaces. The solution to the equilibrium problem is found by constructing a finite set of flux surfaces, each denoted by a flux function  $\psi$ , and adjusting those surfaces until they are in equilibrium.

These flux surfaces are represented by line segments, whose junctions are interconnected to construct a triangular grid. The triangular gridding scheme allows the coordinate system to be tailored to the problem being investigated. Complex geometries and interfaces, multiple magnetic axes, separatrices and limiters (conductors intersecting flux surfaces) are readily accommodated with this model. It is a trivial matter to vary the resolution across the grid and thus provide high resolution only where it is needed. This saves both storage and computing time.

Once the choice of geometries to be investigated has been made, the flux surfaces are generated and tessalated in a semi-automatic fashion. The initial physical parameters are specified and the system is iterated to an equilibrium state in a Lagrangian fashion. A Lagrangian algorithm was chosen for its simplicity and to follow the spatial motion of the flux surfaces under different initial conditions.

When an equilibrium state is reached, the code shifts into the Eulerian portion of the model and the transport and diffusion equations are solved. Diffusion and transport involve rapid flow along the magnetic surfaces, especially those connected to the limiter, so that mass, energy and magnetic flux are transported across the cell boundaries to avoid a severe distortion of the grid that might result with a Lagrangian calculation.

The Lagrangian force balance portion of the model has been discussed in detail in Ref. 6. Some additional general remarks are made below. This report is primarily concerned with the Eulerian transport

portion of this model and the application of this model to the investigation of an axisymmetric poloidal divertor system.

The divertor's function is to remove impurities from the exterior of a magnetically confined plasma. Divertor efficiency depends on the ability of the plasma in the scrape-off layer to stream into the divertor throat, dumping the impurities onto the limiter. With this model, we investigate the physics of the scrape-off layer and the limiter by calculating the plasma flux into the divertor throat and the effect of charge-exchange in the scrape-off layer. The limiter must be able to remove impurities permanently. Our objective is to determine the factors influencing limiter action, and the importance of features such as a neutral blanket on the operation of the limiter.

A short review of the Lagrangian portion of the model is in order. As mentioned above, the model is based on the quasi-static evolution of force-balance in the plasma. The Lagrangian force-balance is presently calculated with only the pressure gradient and the  $\underline{j} \times \underline{B}$  forces (including the toroidal and poloidal magnetic fields). The mass, the entropy and the magnetic fluxes are all conserved as the vertices are adjusted in position in response to any force imbalance. The degree of adjustment is directly proportional to the degree of force imbalance. This adjustment produces a negative definite change in potential energy ensuring the approach to a minimum energy state.

The initial conditions depend on the problem to be solved. We usually prescribe the initial pressure, density and temperature profiles. These functions are then adiabatically adjusted as the

flux surfaces are moved. The magnetic fluxes remain conserved during the Lagrangian motion.

The initial pressure distribution is prescribed as a function of the flux surface variable  $\psi$ . The pressure must remain independent of the poloidal variable on all flux surfaces not connected to the limiter. The pressure is updated adiabatically ( $pV_f^{\gamma} = \text{constant}$ ) on these flux surfaces where  $V_f$  is the volume enclosed by the flux surface. The pressure is updated adiabatically ( $pV_i^{\gamma} = \text{constant}$ ) on the outer surfaces (those connected to a limiter) vertex by vertex. Here  $V_i$  is the volume of the basic cell surrounding the vertex  $i$ .

The toroidal magnetic field is initially prescribed as a function of  $1/R$  over the whole system. As the system is iterated to equilibrium, the toroidal flux is conserved while ensuring  $RB_{\theta} = \text{constant}$  in the vacuum region and  $RB_{\theta} = F(\psi)$  only in the plasma. The  $\psi$  dependence of  $F$  gives the deviation of the toroidal field from the vacuum field and thus measures the poloidal current. The assumption of axisymmetry coupled with the triangular mesh allow the currents to be determined in closed form.

The initial poloidal flux is calculated from the desired toroidal current distribution. The poloidal flux is then conserved throughout the iteration to force balance. Equilibrium states have been obtained for both low and high poloidal beta discharges and for doublet-like and poloidal divertor systems.<sup>10</sup>

There are several important advantages to this model compared to the usual MHD equilibrium model. (1) By focussing on the flux surfaces we avoid the difficulty of having to directly solve a highly non-linear, elliptic partial differential equation with complicated boundary conditions. (2) Complicated geometries with interfaces and separatrices can be accommodated with a minimum of difficulty. (3) The poloidal current distribution is induced in a self-consistent manner so as to ensure force balance. (4) The Eulerian-Lagrangian nature of the model allows both the gross dynamics of the plasma, and the diffusion and transport to be followed. (5) The finite resistivity of the plasma and shell permit the simulation of discharges for times exceeding the penetration time of magnetic fields through the shell.

In the next section we present a detailed discussion of the Eulerian transport model. These equations are expressed on a triangular mesh in Section III. In Section IV, we discuss time scales associated with the problem and the approximations that stem from the ordering of those time scales. In Section V, we present a simple analytical model involving transport along the flux surfaces connected to the limiter (the scrape-off layer). Numerical results are presented in Section VI, with a summary and conclusions in the last section.

## II. PHYSICAL MODEL

### A. Transport

Four fluid equations are needed to describe the dynamics of a two-temperature plasma. The continuity equation is

$$\frac{d\rho}{dt} + \nabla \cdot (\rho \underline{v}) = 0. \quad (\text{II-1})$$

The momentum equation is

$$\rho \frac{dv}{dt} = - \nabla p + \frac{1}{c} \underline{j} \times \underline{B} - \underline{F}_\eta - \underline{F}_{cx}, \quad (\text{II-2})$$

where  $\underline{F}_\eta$  is the viscous drag, and  $\underline{F}_{cx}$  is the ion momentum change resulting from charge exchange. The energy equations are

$$\begin{aligned} n \frac{\partial T_i}{\partial t} = & - n \nabla \cdot (T_i \underline{v}_i) + (2-\gamma) n T_i \nabla \cdot \underline{v}_i - \nabla \cdot (\underline{q}_i) + Q_\eta - Q_{cx} \\ & + \frac{3M_e n}{M_i \tau_e} (T_e - T_i), \end{aligned} \quad (\text{II-3})$$

and

$$\begin{aligned} n \frac{\partial T_e}{\partial t} = & - n \nabla \cdot (T_e \underline{v}_e) + (2-\gamma) n T_e \nabla \cdot \underline{v}_e - \nabla \cdot (\underline{q}_e) + \frac{j_b^2}{\sigma_b} \\ & + \frac{j_\perp^2}{\sigma_\perp} - \frac{0.71}{e} \underline{j} \cdot \nabla_b T_e - \frac{3M_e n}{M_i \tau_e} (T_e - T_i), \end{aligned} \quad (\text{II-4})$$

where  $Q_\eta$  is the heat generated by the viscous drag,  $Q_{cx}$  is the energy lost by charge exchange, the symbol  $b(\perp)$  indicates the direction parallel (perpendicular) to the total magnetic field and  $\underline{q}_i(\underline{q}_e)$  is the ion (electron) heat flux.

The viscous drag, charge exchange and heat flux terms are as yet unspecified. For the calculations which follow, we have taken

$$\underline{F}_\eta = \nabla \cdot \underline{\pi} \quad (\text{II-5})$$

where  $\underline{\pi}$  is the viscous stress tensor,<sup>11</sup> the components of which are presented in the Appendix.

$$\underline{F}_{\text{cx}} = n_0 m_0 \underline{c}_{\text{cx}} \frac{\underline{v}}{|\underline{v}|}, \quad (\text{II-6})$$

where

$$c_{\text{cx}} = 7.6 \times 10^{-3} - 1 \times 10^{-3} \log \left[ \frac{1}{2} n v_{\text{rel}}^2 (\text{ev}) \right]^{1/2} \text{ cm}^2, \quad (\text{II-7})$$

and

$$\underline{Q}_\eta = \underline{\pi} : \underline{Vv}$$

$$Q_{\text{cx}} = n_0 m_0 \underline{c}_{\text{cx}} (V_{\text{rel}})^3. \quad (\text{II-8})$$

$$\underline{q}_i = -K_{ib}^i \nabla_i T_i - K_{ii}^i \nabla_i T_i - K_{ib}^i \times \nabla_i T_i;$$

$$\underline{q}_e = -K_{eb}^e \nabla_e T_e - K_{ee}^e \nabla_e T_e - K_{eb}^e \times \nabla_e T_e;$$

where  $K^i (K^e)$  is the classical ion (electron) thermal conductivity,<sup>11</sup>

and  $V_{\text{rel}}$  is the relative velocity between the neutral and ionic species.

The motion and geometry are completely determined by four more equations. One is Ohm's law, including the electron pressure and Hall terms

$$\underline{E} + \frac{1}{c} \underline{V} \times \underline{B} = \frac{j_b}{\sigma_b} + \frac{j_\perp}{\sigma_\perp} + \frac{1}{nec} \underline{j} \times \underline{B} - \frac{1}{ne} \nabla p_e. \quad (\text{II-9})$$

We need three of Maxwell's equations,

$$\nabla \cdot \underline{B} = 0, \quad (\text{II-10})$$

$$\frac{\partial}{\partial t} \int \underline{B} \cdot d\underline{S} = -c \oint \underline{E} \cdot d\underline{l}, \quad (\text{II-11})$$

$$\oint \underline{B} \cdot d\underline{l} = \frac{4\pi}{c} I, \quad (\text{II-12})$$

where we use the integral forms of Faraday's and Ampère's laws. These equations are solved in an axisymmetric orthogonal flux coordinate system described in the next section.

We seek to solve this set of equations on the resistive diffusion timescale, which is long compared to the Alfvén transit time. On the resistive time scale the inertial terms in the momentum equation are negligible and the system evolves through a series of quasi-static equilibrium states satisfying the static force balance condition

$$\nabla p = \frac{1}{c} \underline{j} \times \underline{B}. \quad (\text{II-13})$$

The method of attaining an equilibrium, by solving Eq. (II-13), is discussed in detail in Ref. 6.

Once an equilibrium state has been obtained, the transport equations



are solved in the following manner:

- (1) The poloidal (toroidal) current is obtained by integrating Ampère's law in the toroidal (poloidal) direction.
- (2) The perpendicular velocity is obtained from Ohm's law.
- (3) The parallel velocity is found by assuming steady-state flow along the flux surface; the parallel pressure gradient is balanced by parallel viscous drag and charge exchange.
- (4) The electric fields are determined from the parallel component of Ohm's law.
- (5) Once the currents, velocities and electric fields are determined, the mass density, the energies and the magnetic fluxes are transported according to Eqs. II - 1, 3, 4 and 11.

The preceding algorithm completely determines the equilibrium plasma properties. The algorithm is outlined in Figure 1. In the next section we discuss the toroidal coordinate system and the differential algebra.

#### B. Coordinate System

We employ spherator-like<sup>13,14</sup> orthogonal basis vectors determined by the poloidal flux. Axisymmetry is assumed so all physical quantities are independent of the toroidal coordinate ( $\theta$ ). Figure 2 illustrates these basis vectors. Following Ref. 14, we introduce a poloidal flux function  $\Psi(R,Z,t)$  defined by

$$\frac{\partial \Psi}{\partial Z} = RB_R, \quad \frac{\partial \Psi}{\partial R} = -RB_Z, \quad (\text{II-14})$$

and a function  $\chi(R,Z,t)$  such that

$$\nabla \Psi \cdot \nabla \chi = 0. \quad (\text{II-15})$$

That is, the surfaces of constant  $\Psi$  are orthogonal to the surfaces of constant  $\chi$ .

The magnetic field is written as

$$\underline{B} = \underline{B}_\chi + \underline{B}_\Psi \quad (\text{II-16})$$

with the poloidal field given by

$$B_\chi^2 = B_R^2 + B_\theta^2. \quad (\text{II-17})$$

The metric of the flux coordinate system  $(\chi, \Psi, \theta)$  is given by

$$(dl)^2 = (B_\chi)^{-2} (d\chi)^2 + (RB_\chi)^{-2} (d\Psi)^2 + R^2 (d\theta)^2. \quad (\text{II-18})$$

This gives rise to the following differential operations

$$\nabla f = \hat{e}_\Psi RB_\chi \frac{\partial f}{\partial \Psi} + \hat{e}_\chi B_\chi \frac{\partial f}{\partial \chi} + \hat{e}_\theta \frac{1}{R} \frac{\partial f}{\partial \theta}, \quad (\text{II-19})$$

$$\nabla \cdot \underline{A} = B_\chi^2 \frac{\partial}{\partial \Psi} \left( \frac{RA_\Psi}{B_\chi} \right) + B_\chi^2 \frac{\partial}{\partial \chi} \left( \frac{A_\chi}{B_\chi} \right) + \frac{1}{R} \frac{\partial A_\theta}{\partial \theta}, \quad (\text{II-20})$$

$$\begin{aligned} \nabla \times \underline{A} = & \hat{e}_\Psi \left[ \frac{1}{R} \frac{\partial A_\chi}{\partial \theta} - \frac{B_\chi}{R} \frac{\partial}{\partial \chi} (RA_\theta) \right] + \hat{e}_\chi \left[ B_\chi \frac{\partial RA_\theta}{\partial \Psi} - \frac{1}{R} \frac{\partial A_\Psi}{\partial \theta} \right] \\ & + \hat{e}_\theta RB_\chi^2 \left[ \frac{\partial}{\partial \chi} \left( \frac{A_\Psi}{RB_\chi} \right) - \frac{\partial}{\partial \Psi} \left( \frac{A_\chi}{B_\chi} \right) \right], \end{aligned} \quad (\text{II-21})$$

$$d\underline{S} = \hat{e}_\Psi \frac{R}{B_\chi} d\chi d\theta + \hat{e}_\chi \frac{1}{B_\chi} d\Psi d\theta + \hat{e}_\theta \frac{1}{RB_\chi^2} d\chi d\Psi, \quad (\text{II-22})$$

$$dV = B_{\chi}^{-1} d\theta d\chi d\psi \quad (\text{II-23})$$

with the derivatives given by

$$RB_{\chi} \frac{\partial}{\partial \psi} = B_R \frac{\partial}{\partial Z} - B_Z \frac{\partial}{\partial R}, \quad (\text{II-24})$$

$$B_{\chi} \frac{\partial}{\partial \chi} = B_Z \frac{\partial}{\partial Z} + B_R \frac{\partial}{\partial R} \quad (\text{II-25})$$

The transport equations are more amenable to solution in a coordinate system with axes parallel and perpendicular to the magnetic field. For this reason we introduce a coordinate system described by

$$\begin{aligned} \hat{e}_b &= \frac{1}{h} (\hat{e}_{\psi} + f \hat{e}_{\chi}), \\ \hat{e}_s &= \frac{1}{h} (f \hat{e}_{\theta} - \hat{e}_{\chi}), \end{aligned} \quad (\text{II-26})$$

and

$$\hat{e}_{\psi} = \hat{e}_{\psi},$$

where  $f = \frac{B_{\chi}}{B_{\theta}}$  and  $h^2 = 1 + f^2$ .  $\hat{e}_{\psi}$  and  $\hat{e}_s$  define the plane perpendicular to the magnetic field direction  $\hat{e}_b$ .

### C. Currents

We divide the current into parallel ( $j_b$ ) and perpendicular ( $j_{\perp}$ ) parts defined by

$$j_b = \frac{B(j \cdot B)}{B^2} \quad (II-27)$$

and

$$j_{\perp} = \frac{B \times (j \times B)}{B^2} = j_{\psi} + j_s, \quad (II-28)$$

and thus

$$j_b = \frac{1}{h} (j_{\psi} + f j_{\chi}), \quad (II-29)$$

$$j_s = \frac{1}{h} (f j_{\psi} - j_{\chi}). \quad (II-30)$$

The above expressions are used in the velocity and field calculations. In the equilibrium calculation there are no unresolved forces along the flux surface, so the  $\psi$ -component of the current density is zero.

Using the integral form of Ampère's law, we obtain the toroidal current ( $I_{\psi}$ ) on the basic cell vertex. All vertex functions are considered constant over the basic cell, so the toroidal current density ( $j_{\psi}$ ) is just the current divided by the cell area. Applying Ampère's law to the toroidal magnetic field and integrating around the torus, we find the poloidal current flux on a triangle side. The  $R, Z$  components of the current density are found on the triangle in a manner similar to the poloidal magnetic field calculation.<sup>6</sup>

There are several significant features of these algorithms. The components of the current density are found in closed form. The toroidal component is independent of the toroidal angle and thus divergence free. Summing the poloidal current fluxes around a triangle yields zero assuring that no current sources are being introduced, and thus

automatically assuring a divergence-free current. The electric field calculation is discussed in the next section.

#### D. Electric fields

The electric fields are determined from the parallel component of Ohm's law

$$\hat{e}_b \cdot \underline{E} = \frac{\hat{e}_b \cdot \underline{j}_b}{\sigma_b} - \frac{1}{ne} \hat{e}_b \cdot \nabla p_e \quad (\text{II-31})$$

Now

$$\underline{E} = -\nabla\phi - \frac{1}{c} \frac{\partial \underline{A}}{\partial t} \quad (\text{II-32})$$

where  $\underline{A}$  is the vector potential induced by the ohmic heating transformer.

Thus

$$\underline{A} = (0, 0, A_\theta). \quad (\text{II-33})$$

The magnetic flux is contained within the core of the transformer, so we have

$$\underline{B} = \nabla \times \underline{A} = 0$$

within the plasma and from Eq. (II-21)

$$A_\theta = A_\theta (R^{-1}) \quad (\text{II-34})$$

Taking the induced potential to be a linear function of time, we have the following expression for the toroidal component of the induced vector potential

$$A_{\theta} = \frac{\alpha t}{R} \quad (\text{II-35})$$

where  $\alpha$  is a constant to be determined from the ohmic heating current.

The toroidal component of the electric field (the inductive field) is then

$$E_{\theta} = - \frac{\alpha}{cR} \quad (\text{II-36})$$

and from Eq. (II-31) we have the expression for the poloidal electric field

$$E_{\chi} = \frac{1}{f\sigma_b} (j_{\theta} + f j_{\chi}) - \frac{B_{\chi}}{ne} \frac{\partial p}{\partial \chi} + \frac{\alpha}{fcR}. \quad (\text{II-37})$$

To find  $E_{\psi}$  we need an expression for the electrostatic potential. Substituting Eq. (II-32) into Eq. (II-31) and assuming the electron temperature is constant on a flux surface (an assumption which will be relaxed in the future) we find

$$\hat{e}_b \cdot \nabla \left( \phi - \frac{T_e}{e} \ln n \right) = - \frac{h j_b}{f \sigma_b} - \frac{\alpha}{c f R}. \quad (\text{II-38})$$

Letting

$$\Phi = \phi - \frac{T_e}{e} \ln n \quad (\text{II-39})$$

and integrating along a flux surface, we obtain the electrostatic potential to within a surface function.<sup>15</sup>

The surface function ( $\bar{\Phi}(\Psi)$ ) is determined by requiring the absence of any net plasma rotation,

$$\oint \rho v_{\chi} \frac{d\chi}{B_{\chi}} = 0. \quad (\text{II-40})$$

This is an expedient, which allows us to avoid excessive complexity. The physically correct determination of  $\bar{\Phi}$  is from a surface integral over the  $\Psi$  component of the force equation.<sup>12</sup>

We use Eqs. (II-46) and (II-47) below to express  $V_{\chi}$  in our magnetic coordinate system. Then applying the above assumption, we have the following expression for the derivative of the surface function

$$\frac{\partial}{\partial \Psi} \bar{\Phi}(\Psi) = - (D(\Psi) - \oint \frac{R\rho}{h^2 f} \frac{d\chi}{B_{\chi}} \frac{\partial}{\partial \Psi} A(\Psi, \chi')) / G(\Psi), \quad (\text{II-41})$$

where

$$D(\Psi) = \oint \frac{\rho}{ch} \frac{d\chi}{B_{\chi}} \left[ f v_b - \frac{c}{h B_{\theta}} \left( \frac{B j_s}{n e c} + \frac{1}{n e} \nabla_{\chi} p_e \right) \right]. \quad (\text{II-42})$$

$$A(\Psi, \chi') = \int_{\chi'}^{\chi} \frac{d\chi}{B_{\chi}} \left( \frac{h j_b}{f \sigma_b} - \frac{E_{\theta}}{f} \right) - \frac{T_e(\Psi)}{e} \ln n(\Psi, \chi'), \quad (\text{II-43})$$

and

$$G(\Psi) = \oint \frac{R\rho}{h^2 f} \frac{d\chi}{B_{\chi}}. \quad (\text{II-44})$$

The  $\Psi$ -component of the electric field is given by

$$\begin{aligned} E_{\Psi}(\Psi, \chi') &= - R B_{\chi} \frac{\partial}{\partial \Psi} \bar{\Phi}(\Psi, \chi') \\ &= R B_{\chi} \frac{\partial}{\partial \Psi} A(\Psi, \chi') - R B_{\chi} \frac{\partial}{\partial \Psi} \bar{\Phi}(\Psi). \end{aligned} \quad (\text{II-45})$$

### E. Velocities

We separate the velocities into a parallel and perpendicular part in the same manner as the currents, thus

$$v_b = \frac{1}{h} (v_\theta + f v_\chi), \quad (\text{II-46})$$

$$v_s = \frac{1}{h} (f v_\theta - v_\chi) \quad (\text{II-47})$$

and

$$\underline{v}_\perp = \underline{v}_\psi + \underline{v}_s \quad (\text{II-48})$$

With these choices,  $(\hat{e}_\psi, \hat{e}_b, \hat{e}_s)$  is a right-handed, orthonormal basis. We shall now express the velocity in its components on this basis.

We obtain the perpendicular components from Ohm's law,

$$\underline{v}_\perp = \frac{c}{B^2} \left[ \underline{E} \times \underline{B} + \frac{1}{\sigma_\perp} \underline{B} \times \underline{j}_\perp B^2 - \frac{1}{ne} \underline{B} \times \nabla p_e \right]. \quad (\text{II-49})$$

This expression has two components which are

$$v_\psi = \frac{c}{B_\theta h^2} \left[ E_\chi - f E_\theta + \frac{h j_s}{\sigma_\perp} + \frac{1}{ne} \nabla_\chi p_e \right] \quad (\text{II-50})$$

and

$$v_s = \frac{c}{B_\theta h} \left[ E_\psi + \frac{B_\theta h}{nec} j_s + \frac{1}{ne} \nabla_\psi p_e \right]. \quad (\text{II-51})$$

Thus  $\underline{v}_\perp$  is determined when  $\underline{j}$ ,  $\underline{E}$  and  $p$  are known.

The parallel velocity is obtained from the parallel component of the momentum equation. Dotting Eq. (II-2) with  $\hat{e}_b$  and assuming the



acceleration term is negligible, i.e., the parallel velocity has attained its terminal value, we have

$$\hat{e}_b \cdot \nabla p = \hat{e}_b \cdot \frac{F}{\eta} + \hat{e}_b \cdot \frac{F}{cx} \quad (\text{II-52})$$

or that the parallel pressure gradient is balanced by the viscous drag and charge exchange terms.

The full viscous stress tensor for this coordinate system is presented in the Appendix. The parallel component of the viscous drag term is

$$(F_{\eta})_b = \hat{e}_b \eta_b \frac{f}{h} B^2 \frac{\partial}{\partial \chi} \left( \frac{\pi_{bb}}{B \chi} \right), \quad (\text{II-53})$$

where  $\pi_{bb}$  is the  $\hat{e}_b \hat{e}_b$  component of the stress tensor and  $\eta_b$  is the parallel viscosity. Keeping the dominant term in the stress tensor, we obtain

$$(F_{\eta})_b = \hat{e}_b \frac{4}{3} \eta_b \frac{f}{h} B^2 \frac{\partial}{\partial \chi} \left( \frac{f}{h} \frac{\partial v_b}{\partial \chi} \right). \quad (\text{II-54})$$

The charge exchange term describes the momentum change due to a charge exchange event. It can be expressed as the product of a coefficient and the relative velocity between the ion and neutral species.<sup>11</sup> The parallel component of this momentum change is

$$(F_{cx})_b = n_o m \sigma_{cx-b} \frac{v}{|v|} \bigg|_b \quad (\text{II-55})$$

where  $m$  is the reduced mass and  $\sigma_{cx}$  is a function of the relative kinetic energy.<sup>11,12</sup>

Equation (II-52) then takes the form

$$\frac{4}{3} \eta_b B_x \frac{\partial}{\partial x} \left( \frac{f}{h} \frac{\partial v_b}{\partial x} \right) = \frac{\partial}{\partial x} p - n_o m \sigma_{cx} \frac{v_b}{b} \left| \frac{v_b}{b} \right| \quad (\text{II-56})$$

which is solved on each flux surface for the parallel velocity on a triangle.

With the velocities determined on the triangles, the mass density is advanced in time on the vertices, through use of the continuity equation. The ion and electron energies are time-advanced using Eqs. (II-3) and (II-4). The integral form of Faraday's law (Eq. (II-11)) is used to find the new magnetic flux. At this point all quantities have been advanced to the new time. A flow chart for the complete algorithm is illustrated in Figure 3. The computational model for these equations is developed in Section III.

### III. COMPUTATIONAL MODEL

#### A. Introduction

The set of equations developed in Section II will be approximated by finite differences on a triangular mesh. The variables in these equations will be represented as triangle, side, or vertex quantities on this mesh. This differencing procedure is somewhat complex. We will illustrate it by discussing some important basic concepts. We begin with the concept of the basic computational cell. Next we define the gradient operator, and finally we will demonstrate the finite

differencing of the nonlinear diffusion equation. Further information on triangular gridding can be found in Refs. 6, 16, 17.

The basic computational cell is the shaded region shown in Fig. 4. It is formed by joining the side bisectors of the triangles surrounding the general vertex. Any physical quantity defined on the vertex is considered to be constant throughout the basic cell, and each triangle surrounding the general vertex contributes 1/3 of its area to the area of the basic cell.

We now illustrate how a gradient is represented in this model. If vertex quantities are linear functions of position, then, given the function  $g_m$  (defined on vertex  $m$ ), the function  $g$  at any other point,  $n$ , say, can be written, without approximation, as

$$g_n = g_m + \underline{R}_n \cdot \nabla g_n \quad (\text{III-1})$$

Here  $\underline{R}_n$  is the vector from the location of  $g_m$  to the chosen point.

Now consider the triangle  $j$  defined by two side vectors  $\underline{S}_i, \underline{S}_{i+1}$  with the vertex-defined quantities  $g, g_i$  and  $g_{i+1}$ . The index  $j$  indicates triangle quantities, the index  $i$  vertex quantities. (See Fig. 5.) Following Ref. 16, the gradient of  $g$ , uniquely defined on the triangle and constant throughout, is

$$\begin{aligned} \nabla g_j &= (g_i - g) \underline{S}_{i+1}^+ - (g_{i+1} - g) \underline{S}_i^+ \\ &= \sum_{i=1}^3 g_i \frac{\hat{n} \times (\underline{r}_{i-1} - \underline{r}_{i+1})}{2A_j} \end{aligned} \quad (\text{III-2})$$

where  $\underline{S}^+$  is the side vector  $\underline{S}$  rotated clockwise by  $\pi/2$  radians, and is shorthand for a cross product with a basis vector. Here  $\hat{n}$  is a unit vector normal to the computational plane and  $A_j$  is the area of the triangle. The conclusion is that gradients may be naturally represented on triangles, and easily calculated on them.

Now consider the nonlinear diffusion equation

$$\frac{\partial g}{\partial t} = \nabla \cdot (\lambda \nabla g) + H, \quad (\text{III-3})$$

where  $g$  is a vertex quantity and  $\lambda$  and  $H$  (the source function) are assumed to be constant throughout a triangle. Again following Ref. 16, we introduce the flux of the diffusing quantity within each triangle as

$$\underline{F}_j = - \lambda_j \nabla g_j. \quad (\text{III-4})$$

Gauss's theorem says the volume integral of the left side of Eq. (III-3) over the basic cell is equal to the integral of the normal component of  $\underline{F}$  over the boundary of the basic cell. The flux contribution  $G_j$  from triangle  $j$  (Fig. 6) is given by

$$G_j = \frac{1}{2} \underline{F}_j \cdot (\underline{S}_{i+1}^+ - \underline{S}_i^+). \quad (\text{III-5})$$

Summing around the central vertex, the finite difference form of Eq. (III-3) is

$$\frac{\Delta g}{\Delta t} = \frac{1}{n} \left[ \sum_{S=1}^n \omega_S (g_i - g)_S + \sum_{j=1}^n a_j H_j \right] \quad (\text{III-6})$$

where the coupling coefficient

$$\omega_S = \frac{1}{2} (\lambda_{j+1} \text{ctn} \theta_{j+1} + \lambda_{j-1} \text{ctn} \theta_{j-1})$$

and the angles  $\theta_{j\pm 1}$  lie opposite the side  $S$  and  $a_j = 1/3 A_j$ . Examination of Fig. 6 will reveal that all these quantities are area or side subelements of a basic cell. Expressions for the divergence, curl and Laplacian operators are presented in Ref. 17. These are all the difference operators we need. We now proceed to represent the equations of Section II on a triangular grid.

#### B. Currents

With the magnetic fields given on the mesh, the currents can be calculated directly from them by using Ampère's law.

The poloidal magnetic field is assumed constant throughout each triangle. Integrating it around the perimeter of a basic cell gives the toroidal current  $(I_\theta)_i$  at the corresponding vertex. As a basic cell (vertex) function,  $I_\theta$  is constant over the cell. Thus the toroidal current density (defined on a triangle) is given by

$$j_\theta = \frac{1}{3} \sum_{i=1}^3 I_{\theta_i} / A_i, \quad (\text{III-7})$$

The poloidal current is found on triangle sides, by integrating the toroidal magnetic field around the torus. The Lagrangian portion of the code assures the physical condition that

$$RB_{\theta} = f(\psi).$$

Thus the  $\psi$  dependence of  $RB_{\theta}$  is a measure of any induced poloidal currents. It gives the deviation of the toroidal field from the vacuum field. To make this quantitative, apply Ampère's law to a triangle side connecting two flux surfaces. The poloidal current flux on that side is

$$I_{\chi_s} = \frac{c}{4\pi} [R_i \phi_i / A_i - R_{i+1} \phi_{i+1} / A_{i+1}], \quad (\text{III-8})$$

where  $\phi_i$  is the toroidal magnetic flux at vertex  $i$ .

$I_{\chi_s}$  is thus the poloidal current flux through a ribbon obtained by revolving a line of length  $ds$  between the  $\psi$  and  $\psi + d\psi$  flux surfaces about the axis of symmetry. This is equivalent to the manner in which the poloidal magnetic flux is calculated<sup>5</sup> and thus the poloidal current density can be determined on the triangles from the relation

$$\underline{j}_{\chi} = \frac{1}{2\pi r} \hat{e}_{\theta} \times \nabla I_{\chi}. \quad (\text{III-9})$$

Again the current density is an average of currents, divided by a triangle area.

The assumption of axisymmetry allows the current densities to be calculated in closed form on the triangular grid. The toroidal current

density is independent of the toroidal coordinate and automatically divergence-free. Since the poloidal current is the same for all sides interconnecting two flux surfaces, summing the currents around the triangle yields zero, assuring that no current sources are being introduced. There are no unresolved forces along the flux surface in the Lagrangian calculation, so the  $\Psi$  component of the current density is zero.

Expressions for the electric field are presented in the next section.

#### C. Electric Fields

Equations (II-36) and (II-37) yield the toroidal and poloidal electric fields as triangle quantities

$$E_{\theta} = - \frac{\alpha}{cR} \quad (\text{III-10})$$

and

$$E_{\chi} = \frac{1}{f\sigma_b} (j_{\theta} + f j_{\chi}) - \frac{1}{neB_{\chi}} \left( B_R \frac{\partial p_e}{\partial R} + B_z \frac{\partial p_e}{\partial z} \right) - \frac{E_{\theta}}{f} \quad (\text{III-11})$$

The procedure for finding  $E_{\Psi}$  is somewhat more involved. All the integral quantities (Eq. II-41) are weighted to the vertices giving the electrostatic potential on the vertex. The gradient of the potential then yields  $E_{\Psi}$  on the triangles.

#### D. Velocities

The perpendicular components of the velocities are calculated as triangle quantities using Eqs. (II-50) and (II-51),

$$v_{\psi} = \frac{c}{B_{\theta} h^2} \left[ E_{\chi} - f E_{\theta} + \frac{1}{\sigma_{\perp}} (f j_{\theta} - j_{\chi}) + \frac{1}{ne B_{\chi}} \left( B_R \frac{\partial p_e}{\partial R} + B_Z \frac{\partial p_e}{\partial Z} \right) \right] \quad (\text{III-12})$$

and

$$v_s = \frac{c}{B_{\theta} h} \left[ E_{\psi} + \frac{B_{\theta}}{nec} (f j_{\theta} - j_{\chi}) + \frac{1}{ne B_{\chi}} \left( B_R \frac{\partial p_e}{\partial Z} - B_Z \frac{\partial p_e}{\partial R} \right) \right] \quad (\text{III-13})$$

The parallel component of the velocity is found by assuming steady-state flow along the flux surface. The parallel pressure gradient is then balanced by the parallel viscous drag and charge exchange terms. This calculation is discussed in greater detail in Sections IV and V.

To facilitate the gradient and divergence operations, the ion (fluid) and electron velocities are decomposed into R- and Z-components

$$v_R^i = v_{\chi} \frac{B_R}{B_{\chi}} - v_{\psi} \frac{B_Z}{B_{\chi}},$$

$$v_Z^i = v_{\chi} \frac{B_Z}{B_{\chi}} + v_{\psi} \frac{B_R}{B_{\chi}},$$

$$v_R^e = v_R^i - \frac{j_{\chi}}{ne} \frac{B_R}{B_{\chi}},$$

and

$$v_Z^e = v_Z^i - \frac{j_{\chi}}{ne} \frac{B_Z}{B_{\chi}}.$$

We now have all the tools we need to solve the transport and diffusion equations.

#### E. Mass and Energy Transport

As noted previously, the transport and magnetic diffusion are Eulerian. The triangles are held fixed in position and the mass,



energies and magnetic fluxes are transported among the cells.

The continuity equation (Eq. II-1) is differenced in the same manner as the diffusion equation of Section IIIA. The new vertex mass density is

$$\rho_i^n = \rho_i^o + \frac{1}{2} \Delta t \sum_{j=1}^n \rho_j (v_z \Delta R' - v_R \Delta Z')_j / \sum_{j=1}^n a_j \quad (\text{III-14})$$

where  $(\Delta R', \Delta Z')_j$  are the components of the side of triangle  $j$  opposite the vertex  $i$ .

The energy equations (Eqs. II-3, II-4) are solved in a similar fashion. We include both the parallel and perpendicular viscous terms. The perpendicular term will be important (because of the long path length) in the scrape-off layer.<sup>18</sup>

$$Q_n = \frac{4}{3} \eta_b \left( \frac{fB}{h} \chi \frac{\partial v_b}{\partial \chi} \right)^2 - \eta' \frac{RB^2}{h} \left( \frac{\partial}{\partial \psi} \frac{h}{B \chi} \right) v_s \left[ RB \chi \frac{\partial v_\psi}{\partial \psi} + \frac{B}{h} \chi \frac{\partial v_s}{\partial \chi} \right] \quad (\text{III-15})$$

Finite-differencing Eq. (II-3), we have new vertex ion temperature

$$T_i^n = T_i^o + \frac{\Delta t}{\sum_{j=1}^n a_j} \left[ -\frac{1}{2} \sum_{j=1}^n T_j D_j + \frac{1}{2} (2-\gamma) T_i^o \sum_{j=1}^n D_j + \frac{1}{3\phi_i} \sum_{j=1}^n K_j^i C_j \right. \\ \left. + \frac{8}{27} \sum_{j=1}^n \eta_{b_j} v_j - \frac{2}{9} \sum_{j=1}^n \eta'_j v'_j + \frac{2}{3} \frac{m_e}{m_i} \sum_{j=1}^n \left( \frac{T_e - T_i}{\tau_e} \right)_j A_j \right] \quad (\text{III-16})$$

where

$$D_j = (v_R \Delta Z' - v_Z \Delta R')_j, \quad (\text{III-17})$$

$$C_j = \left[ \frac{1}{B_\chi^2} \left( B_R \frac{\partial T}{\partial R} + B_Z \frac{\partial T}{\partial Z} \right) (B_R \Delta Z' - B_Z \Delta R') \right]_j, \quad (\text{III-18})$$

$$V_j = \left[ \frac{1}{\rho B^2} \left( B_R \frac{\partial v}{\partial R} + B_Z \frac{\partial v}{\partial Z} \right)^2 \right]_j A_j, \quad (\text{III-19})$$

$$V'_j = \left[ \frac{1}{\rho B_\chi h} \left( B_R \frac{\partial}{\partial Z} \left( \frac{h}{B_\chi} \right) - B_Z \frac{\partial}{\partial R} \left( \frac{h}{B_\chi} \right) \right) \left[ \left( B_R \frac{\partial v_\psi}{\partial Z} - B_Z \frac{\partial v_\psi}{\partial R} \right) + \frac{1}{h} \left( B_R \frac{\partial v_s}{\partial R} + B_Z \frac{\partial v_s}{\partial Z} \right) \right] \right]_j A_j, \quad (\text{III-20})$$

and  $K^i$  and  $\eta_i$  can be found in Section II.

The magnetic flux is integrated forward in time using the integral form of Ampère's law

$$\frac{\partial}{\partial t} \Phi = - c \oint \underline{E} \cdot d\underline{\ell} \quad (\text{III-21})$$

where

$$\Phi = \int \underline{B} \cdot d\underline{A}$$

The new toroidal electric field is defined on the vertices. Integrating this field around the torus, the new poloidal magnetic flux through a triangle side is

$$\psi_s^n = \psi_s^o + 2\pi c \Delta t (R_i E_{\theta_i} - R_{i+1} E_{\theta_{i+1}}) \quad (\text{III-22})$$

where  $i, i+1$  are the vertices at the ends of side  $s$ . The  $\nabla \cdot \underline{B} = 0$  condition is assured since the sum of the fluxes around a triangle<sup>5,6</sup> is zero.

We wish to keep the toroidal flux a vertex quantity, so Eq. (III-21) is integrated around the basic cell to give the new toroidal flux

$$\phi_i^n = \phi_i^o + \frac{\Delta t c}{2} \sum_{j=1}^n \left[ E_{\chi_j} \left( \frac{B_R \Delta R}{B_{\chi}} + \frac{B_Z \Delta Z}{B_{\chi}} \right)_j - E_{\psi_j} \left( \frac{B_Z \Delta R}{B_{\chi}} - \frac{B_R \Delta Z}{B_{\chi}} \right)_j \right] \quad (\text{III-23})$$

Now that the mass, energy and magnetic flux have been transported, the system is no longer in equilibrium so we return the Lagrangian portion of the code to iterate to a new equilibrium state. The new transport coefficients are found, and the code reenters the transport portion of the model.

#### F. Exactness of Conservation Equations

The basic computational cell is irregular (see Fig. 7). Therefore one might question whether conservation equations can be accurately represented by finite difference operations on these cells. This section shows that accurate representations are used in the present model.

Probably the simplest numerical question is the order of accuracy of a difference algorithm on a triangular grid. Fritts<sup>15</sup> has demonstrated second-order accuracy for a wave equation. We use his methods in this code.

A second natural question is whether "conserved quantities" are conserved to machine roundoff. If this property is desired (and the authors believe it is in this case), it can easily be accomplished by expressing the changes in the conserved quantities in terms of fluxes between the cells, and insuring that the flux is calculated in the same way from both "sides" at a cell boundary. This is done in the code.

There is another important aspect to "conservation" in a magnetic geometry. It is conservation within a flux surface. In a tokamak-like system, the velocity components in the magnetic surfaces may be two or three orders of magnitude larger than the component perpendicular to the surface. Thus a numerical algorithm may seriously degrade conservation of energy (or density) in a flux surface, if it allows even a small part of the surface velocity to appear as a normal velocity in the different equations. The remainder of this section explains how this problem is avoided in a triangular gridding system.

Consider a Gedanken experiment where the temperature is zero

everywhere except at one vertex. There it is  $T'$ . A set of flux surfaces is illustrated in Figure 7a. We will show that our Eulerian scheme, for advancing the energy and mass densities forward in time, preserves the physics of the conservation equations; i.e., that the parallel and perpendicular transports are completely uncoupled.

In our Gedanken experiment we shall consider parallel heat flux in the energy equation, and show that no energy is transported between flux surfaces. The energy equation has the form

$$\frac{\partial T}{\partial t} = \nabla \cdot \underline{q}_b = - \nabla \cdot (\underline{K}_{bb} \cdot \nabla T) \quad (\text{III-23})$$

where  $\underline{K}_{bb}$  is the parallel conductivity tensor. From Eq. (III-2), the temperature gradient is zero everywhere except for the triangles around vertex "a" where it is normal to the sides opposite vertex "a".

Finite differencing Eq. III-23 on vertex "c", we have

$$\frac{\Delta T_c}{\Delta t} = \frac{1}{2A_c} \sum_{j \in \odot} \underline{q}_{bj} \cdot (\hat{n} \times \underline{S}_{oc}). \quad (\text{III-24})$$

For triangles 1. and 4., the parallel heat flux is zero since the temperature gradient is normal to the flux surface. For triangle 2., the parallel heat flux is normal to the surface area vector of the basic cell. Thus if we are solving for the parallel transport, we are assured that no energy is being transported across the flux surface numerically

The mass continuity equation also exactly conserves density. Here we assume the density is zero everywhere except at one vertex and assume only flow in the magnetic surface. See Figure 7b. The continuity

equation has the form

$$\frac{\Delta \rho_c}{\Delta t} = - \frac{1}{2A_c} \sum_{j \in \textcircled{C}} \rho_j \vec{v}_j \cdot (\hat{n} \times \underline{S}_{oc}) \quad (\text{III-25})$$

where  $\rho_j$  (the density on the triangle) is the average of the densities at the vertices of the triangle. From Eq. II-56, we see that the parallel velocity is a function of the parallel component of the pressure gradient. For triangles 1. and 4., the parallel velocity is zero. The parallel flux of triangle 2 is again normal to the surface of basic cell c, and no mass is transported across the flux surface.

Finally, we may assure that if we have only perpendicular flow, no mass is transported along a flux surface. Considering only perpendicular flow, the change in the mass density at vertex b is

$$\frac{\Delta \rho_b}{\Delta t} = - \frac{1}{2A_b} \sum_{j \in \textcircled{B}} \rho_j \vec{v}_{\perp j} \cdot (\hat{e}_\theta \times \underline{S}_{ob}) \quad (\text{III-26})$$

where  $p_j = 1/3 p'$ . See Figure 8.

Now

$$\vec{v}_{\perp} = v_\psi \hat{e}_\psi + v_s \hat{e}_s,$$

and the velocity arising directly from the pressure is

$$v_\psi = \mu \hat{e}_\chi \cdot \nabla p$$

and

(III-27)

$$v_s = h \mu \hat{e}_\psi \cdot \nabla p$$

(c.f. Eqs. II-50, 51) where

$$\mu = \frac{c}{neBh}.$$

the perpendicular velocity can then be expressed as

$$\underline{v}_\perp = \mu \hat{e}_\theta \times \nabla p. \quad (\text{III-28})$$

Letting  $F_j$  be the flux contribution from each of the triangles surrounding vertex  $b$ , we have for triangles 2 and 3 respectively

$$F_2 = \frac{1}{3} \rho' \mu \nabla p_2 \cdot \underline{S}_1 \quad (\text{III-29})$$

and

$$F_3 = \frac{1}{3} \rho' \mu \nabla p_3 \cdot \underline{S}_4 \quad (\text{III-30})$$

with the pressure gradients given by

$$\nabla p_2 = \frac{\rho'}{2A_2} \hat{e}_\theta \times \underline{S}_3 \quad (\text{III-31})$$

and

$$\nabla p_3 = \frac{\rho'}{2A_3} \hat{e}_\theta \times \underline{S}_5. \quad (\text{III-32})$$

$A_2$  and  $A_3$  are the triangle areas,

$$A_2 = \frac{1}{2} \hat{e}_\theta \cdot (\underline{S}_3 \times \underline{S}_1)$$

and

$$A_3 = \frac{1}{2} \hat{e}_\theta \cdot (\underline{S}_4 \times \underline{S}_5).$$

Substituting into Equation III-26 and summing around vertex  $b$  we have

$$\frac{\Delta p_b}{\Delta t} = \frac{\rho'^2 \mu}{12A_b} \left[ \frac{\hat{e}_\theta \cdot (\underline{S}_3 \times \underline{S}_1)}{A_2} + \frac{\hat{e}_\theta \cdot (\underline{S}_5 \times \underline{S}_4)}{A_3} \right] \quad (\text{III-33})$$

which is identically zero.

A similar argument applies to the perpendicular heat flux since the conductivity tensor contains both a  $\psi$  and an  $s$  component.

The power of the triangular gridding scheme is immediately evident. Not only can complicated geometries be modified with a high degree of resolution, but the gradient operator, as a triangle function, is exact and there is absolutely no numerical coupling between the parallel and perpendicular transport.

#### G. Summary

We now summarize the transport calculation. The toroidal and poloidal components of the current density are found as triangle quantities from Ampère's law.

The poloidal and toroidal electric fields are found as triangle quantities from the parallel component of Ohm's law.

Once the parallel fields and current densities are known, the perpendicular components of the velocity are determined as triangle quantities from the perpendicular component of Ohm's law. The parallel component is determined as a triangle quantity by equating the parallel viscous drag and charge exchange with the parallel pressure gradient.

The perpendicular electric field is then found by solving the parallel component of Ohm's law for the electrostatic potential under the condition that there is no net plasma rotation.

Now that the dynamical variables have been determined, the transport equations are solved to give the new mass densities and energies on the vertices and the new toroidal (poloidal) flux as a vertex (side) quantity.

In the next section we discuss a reduced set of equations that stem from an examination of the time scales associated with this problem.



#### IV. SIMPLIFIED MODEL

##### A. Time Scales

Our model is based on the assumption that the equations presented in the last two sections can be solved on the resistive time scale ( $\tau_o$ ). Since the resistive time scale is much larger than the Alfvén ( $\tau_A$ ) time scale, the inertial terms in the equation of motion are negligible and the system can be taken as evolving through a sequence of equilibrium states satisfying the force-balance condition. By comparing the characteristic times for the other dissipative processes with the Alfvén transit time, we find that density and temperature perturbations on a magnetic flux surface cannot be maintained for times on the order of the Alfvén transit time.

The Alfvén transit time is given by

$$\tau_A = \frac{a}{(B^2/4\pi\rho)^{1/2}}, \quad (\text{IV-1})$$

where  $a$  is the plasma radius. The characteristic times for the important dissipative processes are:

Resistive diffusion,

$$\tau_o \sim L^2/D_B \sim \frac{4\pi o L^2}{c^2} \quad (\text{IV-2})$$

Particle diffusion,

$$\tau_D \sim \frac{L^2 m_i}{\tau_i T_i}, \quad (\text{IV-3})$$

Thermal conduction,

$$\tau_K \sim \frac{L^2 n}{K} \quad (\text{IV-4})$$

and for viscous drag

$$\tau_\eta \sim \frac{L^2 \rho}{\eta}, \quad (\text{IV-5})$$

where  $L$  is a characteristic scale length and  $\tau_i$  is the ion-ion collision time.

Comparing the resistive diffusion time to the Alfvén transit time,

$$\frac{\tau_\sigma}{\tau_A} \approx \sqrt{\beta} \frac{\Omega_i}{v_i} \frac{a}{\rho_e} \gg 1. \quad (\text{IV-6})$$

where  $\beta = nT/(B^2/8\pi)$ ,  $\Omega_i = eB/m_i c$ ,  $\rho_e = v_{the}/\Omega_e$  and  $v_i$  is the ion-ion collision frequency. The criterion required for our basic assumption to be met is thus well satisfied.

Comparing the characteristic times of the other dissipative processes along the flux surfaces to the Alfvén time, we have

$$\tau_D^{\parallel}/\tau_A \sim \tau_A^{\parallel}/\tau_A \sim \tau_\eta^{\parallel}/\tau_A \sim \frac{1}{\sqrt{\beta}} \frac{v_i}{\Omega_i} \ll 1. \quad (\text{IV-7})$$

The above implies that density, temperature and velocity perturbations cannot exist on a flux surface for times on the order of the Alfvén transit time; thus, to a very good approximation the density and temperature can be taken to be constant on a flux surface. This applies

to all flux surfaces except for the separatrix and the scrape-off layer where the parallel transport must be determined. This problem is addressed in Sections IV.C and V.

#### B. Perpendicular Transport

As an examination of the time scales indicates, the particle and heat flux is very rapid along the flux surfaces compared to the resistive diffusion across the surfaces. To lowest order then, we need only solve for the perpendicular transport and take the parallel transport as occurring with infinite speed.

Our simplified model then consists of including only the perpendicular transport coefficients (cf. Eq. II-8). Once the continuity and energy equations have been solved, the density and temperatures are averaged on the flux surfaces. The only modifications to the equations presented in the previous two sections are that all the parallel transport coefficients are set to zero.

In the next section we discuss the parallel transport in the scrape-off layer where this approximation cannot be made.

#### C. Simplified Transport Equations

In the interior of the discharge, the ordering discussed in the previous section insure that temperature and pressure are constant on each magnetic surface. As one proceeds outward toward the limiter, the effect of the external boundaries is to increase transport in the surfaces, and perturb this equilibrium.

The pressure and temperature distributions on the outer surfaces are still nearly constant, but they exhibit some variation on these

surfaces, accompanied by very rapid transport on the (resistive) times of interest to us. Thus it is appropriate to calculate the transport in the outer surfaces by determining the fluxes across magnetic surfaces from the averaged quantities, and to determine the transport in the surfaces from the quasi-stationary solutions of the equations including surface variations.

We shall assume that this outer region is cold enough that viscosity is no longer important, and that the neutral density is sufficiently high that Ohmic heating is negligible. Then equations (II-1 to 4) reduce to

$$\nabla \cdot (n\mathbf{v}) = S, \quad (\text{IV-8})$$

$$\nabla p - \frac{1}{c} \mathbf{j} \times \mathbf{B} + mn\mathbf{v}/\tau_{cx} = 0, \quad (\text{IV-9})$$

$$n\nabla \cdot (T_i \mathbf{v}_i) - (2-\gamma)nT_i \nabla \cdot \mathbf{v}_i = -\nabla \cdot (\mathbf{q}_i) - Q_{cx} + \frac{3m_e n}{m_i \tau_e} (T_e - T_i) \quad (\text{IV-10})$$

and

$$n\nabla \cdot (T_e \mathbf{v}_e) - (2-\gamma)nT_e \nabla \cdot \mathbf{v}_e = -\nabla \cdot (\mathbf{q}_e) - \frac{3m_e n}{m_i \tau_e} (T_e - T_i) - \frac{0.71}{e} \mathbf{j}_p \cdot \nabla T_e \quad (\text{IV-11})$$

Here  $\tau_{cx}$  is the charge-exchange time and  $S$  represents a source term.

Ohm's law plays an important role in this region, since an electrostatic potential is required near the limiter to enforce ambipolarity. To be consistent with the preceding assumptions, we must neglect the conductivity and ohmic heating vector potential terms. We also neglect the electron pressure and Hall terms. Then Eq. (II-9) becomes

$$-\nabla\phi + \frac{1}{c} \underline{j} \times \underline{B} = n\underline{j} \quad (\text{IV-12})$$

with  $\phi$  the electrostatic potential.

With  $\underline{B}$  determined separately and using the zeroth order current densities as determined from Ampère's law, equations (IV-8) through (IV-12) plus charge conservation

$$\nabla \cdot \underline{j} = 0 \quad (\text{IV-13})$$

can be solved for the first order quantities  $p$ ,  $T_e$ ,  $T_i$ ,  $\phi$ ,  $\underline{v}$  and  $\underline{j}$ . This solution is discussed in the next section.

## V. AN ANALYTIC BENCHMARK

### A. Ordering

The solutions of the transport equations in the exterior will include rapid flow and heat flux along  $B$  toward the limiter. Little else is easy to discern from the transport equations. Thus it is appropriate to reduce these equations to an analytically tractable form. This can most easily be done by assuming only small variations on the surfaces. We assume that  $n$  and  $T$  satisfy inequalities like

$$\frac{L}{n} \frac{\partial n}{\partial y} \sim \epsilon \ll 1 \quad (\text{V-1})$$

where  $y$  is a measure of length in the poloidal direction and  $\oint dy = L$ . For simplicity we shall also assume  $T_e = T_i = T$ , and examine only one temperature equation. Then the equations we wish to solve are

$$\nabla \cdot (n\underline{v}) = S, \quad (\text{V-2})$$

$$\nabla \cdot \underline{j} = 0, \quad (\text{V-3})$$

$$(\underline{w} - \frac{\underline{j}}{en} + \frac{0.71}{2en} \underline{j} \cdot \hat{e}_b \hat{e}_b) \cdot \nabla T + (\gamma-1) n T \nabla \cdot (\underline{w} - \frac{\underline{j}}{en})$$

$$- \nabla \cdot [ \hat{e}_\psi \times (\hat{e}_\psi \times \underline{K} \cdot \nabla T) ] \quad (V-4)$$

$$= - \hat{e}_\psi \cdot [ n \underline{v}_\psi \nabla T + (\gamma-1) n T \nabla \underline{v}_\psi - \nabla \hat{e}_\psi \cdot \underline{K} \cdot \nabla T ],$$

$$- \nabla \phi + \frac{1}{c} \underline{v} \times \underline{B} - \eta \underline{j} = 0 \quad (V-5)$$

and

$$\nabla p - \frac{1}{c} \underline{j} \times \underline{B} + mn \underline{V} / \tau_{cx} = 0, \quad (V-6)$$

where  $\underline{w} = \hat{e}_\psi \times \underline{v} \times \hat{e}_\psi$  represents the two-velocity components in the magnetic surface. We now examine them order by order.

Represent each of these nine physical variables by a series in  $\epsilon$ , for example,

$$n = n^{(0)} + \epsilon n^{(1)} \dots \quad (V-7)$$

Assume the source terms are first order in  $\epsilon$ . Further, assume that the zero-order density and temperature are surface functions. Then equations

(V-2) - (V-6) reduce to

$$\nabla \cdot \underline{w}^{(0)} = 0, \quad (V-8)$$

$$\nabla \cdot \underline{j}^{(0)} = 0, \quad (V-9)$$

$$\nabla n^{(0)} k T^{(0)} - \frac{1}{c} \underline{j}^{(0)} \times \underline{B}^{(0)} + mn \underline{w}^{(0)} / \tau_{cx} = 0 \quad (V-10)$$

$$- \nabla \phi^{(0)} - \eta \underline{j}^{(0)} + \frac{1}{c} (\underline{w}^{(0)} - \frac{\underline{j}^{(0)}}{en^{(0)}} \times \underline{B}) = 0, \quad (V-11)$$

plus an energy equation which vanishes identically.

These equations may be solved as follows. Equation (V-8) may be integrated, yielding a velocity vector with a prescribed poloidal variation, plus a constant vector in the ignorable direction. The parallel component of Eq. (V-10) requires the parallel component of  $\underline{w}$  to vanish. The only consistent solution is

$$\underline{w}^{(0)} = 0. \quad (V-12)$$

By similar analysis, the integral of Eq. (V-9) and the perpendicular component of Eq. (V-10) uniquely determine

$$\underline{j}^{(0)} = \frac{cB^{(0)} \times \nabla n^{(0)} kT^{(0)}}{B^2} \quad (V-13)$$

and finally, from Eq. (11),

$$\nabla \phi^{(0)} = - \eta \underline{j}^{(0)} \quad (V-14)$$

This completely determines the lowest order solution.

#### B. First-Order Equations

In this ordering, the flow and surface variations of density and temperature appear in first order. We shall represent the density and temperature source terms through sources  $S$  and  $q$  which are given.

Then the first-order equations are

$$B_{\chi}^2 \frac{\partial}{\partial \Psi} \left( \frac{R n^{(0)} v_{\Psi}}{B_{\chi}} \right) + n^{(0)} B_{\chi}^2 \frac{\partial}{\partial \chi} \left( \frac{v_{\chi}}{B_{\chi}} \right) = \underline{S} \quad (V-15)$$

$$B_{\chi}^2 \frac{\partial}{\partial \Psi} \left( \frac{R j_{\Psi}}{B_{\chi}} \right) + B_{\chi}^2 \frac{\partial}{\partial \chi} \left( \frac{j_{\chi}}{B_{\chi}} \right) = 0 \quad (V-16)$$

$$- \hat{e}_{\Psi} \nabla_{\Psi} p + \frac{1}{c} (j_{\chi} B_{\theta} - j_{\theta} B_{\chi}) \hat{e}_{\Psi} - \frac{m n^{(0)}}{\tau} v_{\Psi} \hat{e}_{\Psi} = 0, \quad (V-17)$$

$$- \hat{e}_{\chi} \nabla_{\chi} p - \frac{1}{c} j_{\Psi} B_{\theta} \hat{e}_{\chi} - \frac{m n^{(0)}}{\tau} v_{\chi} \hat{e}_{\chi} = 0, \quad (V-18)$$

$$\hat{e}_{\theta} \frac{1}{c} j_{\Psi} B_{\chi} - \frac{m n^{(0)}}{\tau} v_{\theta} \hat{e}_{\theta} = 0, \quad (V-19)$$

$$- \hat{e}_{\Psi} \nabla_{\Psi} \phi + \frac{1}{c} (v_{\chi} B_{\theta} - v_{\theta} B_{\chi}) \hat{e}_{\Psi} = 0, \quad (V-20)$$

$$- \hat{e}_{\chi} \nabla_{\chi} \phi - \frac{1}{c} (v_{\Psi} B_{\theta}) \hat{e}_{\chi} - \eta j_{\chi} \hat{e}_{\chi} = 0 \quad (V-21)$$

and

$$\frac{1}{c} v_{\Psi} B_{\chi} \hat{e}_{\theta} - \eta j_{\theta} \hat{e}_{\theta} = 0 \quad (V-22)$$

We take  $j_{\theta}^{(0)}$  and  $j_{\chi}^{(0)}$  as given quantities as determined from Ampere's law. The previous set of equations is then solved in the following manner.

From Eq. (V-22)

$$v_{\Psi} = \frac{c \eta j_{\theta}}{B_{\chi}} \quad (V-23)$$



The electrostatic potential is found from Eq. (V-21),

$$\frac{\partial \phi}{\partial \chi} = - \frac{n h j_b}{B \chi f} . \quad (V-24)$$

The other velocity components are then found from Eqs. (V-15) and (V-20),

$$\frac{\partial}{\partial \chi} \left( \frac{v_\chi}{B \chi} \right) = \frac{S}{n^{(0)} B \chi^2} - \frac{c}{n^{(0)}} \frac{\partial}{\partial \psi} \left( \frac{n R j_\theta n^{(0)}}{B \chi^2} \right) \quad (V-25)$$

and

$$v_\theta = \frac{1}{f} v_\chi - c R \frac{\partial \phi}{\partial \psi} . \quad (V-26)$$

The  $\psi$  and  $\chi$  components of the first order current densities are given by Eqs. (V-19) and (V-10),

$$j_\psi = \frac{c m n^{(0)}}{B \chi \tau} v_\theta \quad (V-27)$$

and

$$\frac{\partial}{\partial \chi} \left( \frac{j_\chi}{B \chi} \right) = - c m \frac{\partial}{\partial \psi} \left( \frac{R n^{(0)}}{B \chi \tau} v_\theta \right) . \quad (V-28)$$

The momentum equation then yields the pressure

$$\frac{\partial p}{\partial \chi} = - \frac{m n^{(0)}}{B \chi \tau f} h v_b \quad (V-29)$$

and the toroidal current density

$$j_\theta = \frac{1}{\left( 1 + \frac{m n^{(0)}}{\tau} \frac{c^2}{B \chi^2} \right)} \left[ \frac{j_\chi}{f} - R c \frac{\partial p}{\partial \psi} \right] \quad (V-30)$$

The remaining equation to solve is the energy equation. Writing  $p^{(1)}$  as  $(n^{(0)} n_T^{(1)} + n^{(1)} n_T^{(0)})$ , it can now be expressed in terms of known quantities.

In other calculations of this nature, consistency conditions determine the integration constants in the velocity and current. Here they are determined by the sheath conditions at the limiter.

### C. Boundary Conditions

Boundary conditions are required for equations (V-24), (V-25), (V-28) and (V-29). These boundary conditions are determined by the limiter.

Integrating Eq. (V-24),

$$\phi(\chi') = - \int_{\chi_\ell}^{\chi'} \frac{\eta h j_b}{B \chi f} d\chi + \phi_\ell \quad (V-31)$$

where  $\phi_\ell$  is the sheath potential at the limiter. This potential will generally be a few Debye lengths ( $\lambda_D$ ) thick and is of the form

$$\phi \sim 4\pi n e \lambda_D^2$$

and thus only a function of the temperature at the limiter.

In a similar manner, Eq. (V-25) gives

$$v_\chi(\chi') = B_\chi(\chi') \int_{\chi_\ell}^{\chi'} \left( \frac{s}{n^{(0)} B_\chi^2} - \frac{c}{n^{(0)}} \frac{\partial}{\partial \psi} \left( \frac{\eta R j_\theta n^{(0)}}{B_\chi^2} \right) d\chi \right) + \frac{B_\chi(\chi')}{B_{\chi_\ell}} v_\ell \quad (V-32)$$

where  $v_\ell$  is the ion-thermal velocity at the limiter.

## VI. NUMERICAL RESULTS

### A. Equilibrium

The initial flux surfaces for the divertor grid are generated by a multicurrent vacuum code with the positions and strengths of external magnetic field coils chosen to be representative of PDX II geometry.<sup>19</sup> Seventeen surfaces are used in the grid (each current axis, defined by a single point, is counted as a separate surface). Each surface is then divided into a number of straight-line segments, the end points of which are the triangle vertex positions. The computer code then automatically generates the triangular grid structure from these vertex positions. The initial grid is shown in Figure 9.

The two outermost surfaces represent the conducting shell (copper). Proceeding inward, the next surface is a vacuum surface, the next two surfaces comprise the scrape-off layer, the next surface is the separatrix and the inner surfaces describe either the plasma discharge or the divertor.

The power of the triangular gridding scheme in providing a mesh with variable resolution is immediately evident. Flow in the scrape-off layer, the region bounded by the separatrix and the plasma-vacuum interface, is expected to be quite rapid and thus this region should be finely resolved. This region is divided into 382 triangles. Flow in the main body of the plasma discharge, the area enclosed by the separatrix and to the right of the null point, should be much less than the flow in the scrape-off layer and thus the region does not need to be so finely resolved. The plasma discharge region, which occupies a much larger area than the scrape-off layer is

represented by 373 triangles. In all, the divertor grid is composed of 17 flux surfaces, 777 vertices, 1458 triangles and 2234 line segments.

Once the grid structure has been generated, the plasma profiles are calculated with the pressure, density, temperatures and plasma current specified on the vertices. The initial current density and temperature profiles are parabolic out to the separatrix. The density profile has a cubic radial dependence. These profiles then fall off nearly exponentially from the separatrix to small but non-zero values at the plasma-vacuum interface. The initial density and temperatures are:

$$n(r = 0) = 9 \times 10^{13} \text{ cm}^{-3}$$

and

$$T_e(r = 0) = T_i(r = 0) = 0.7 \text{ KeV.}$$

At the plasma-vacuum interface

$$n = 1.7 \times 10^{12} \text{ cm}^{-3}$$

and

$$T_e = T_i = 0.01 \text{ KeV.}$$

The system is then iterated to an equilibrium state as discussed in Section I of this report and in detail in Ref. 6. The toroidal magnetic field is slowly ramped over 10 iteration steps to its final value of 20 KG. Depending on the initial plasma parameters, the system attains equilibrium after 100-150 iteration steps.

The equilibrium grid structure is presented in Figure 10 with the corresponding profiles in Figures 11-13. The plasma current has a value of 990 KA and the central density and temperatures are

$$n(r = 0) = 9.3 \times 10^{13} \text{ cm}^{-3}$$

and

$$T_e(r = 0) = T_i(r = 0) = .8 \text{ KeV.}$$

The major radius is 123 cm and the minor radius is 60 cm. The poloidal beta is 0.7. The width of the scrape-off layer (at the null point) on the outside of the separatrix is 16 cm and the width on the inside is 22 cm. The perimeter of the plasma discharge has a length of 370 cm (see Figure 14). The results of the transport calculation are presented in the next section.

## B. Transport

Now that an equilibrium state has been attained, the diffusion and transport equations can be solved. Before presenting the results of this calculation several remarks are in order.

As noted in Section I, one-dimensional transport calculations which necessitate the determination of flux surface averaged quantities are not appropriate for investigating the divertor system. This is because the surface integrals generally involve terms of the form  $B_{\chi}^{-1}$  and the poloidal field ( $B_{\chi}$ ) goes to zero at the null point on the separatrix. Without a careful choice of computational grid and metric, most surface averaged quantities are formally infinite on the separatrix.

This difficulty is avoided completely in our computation for several reasons. First, the calculation is fully two-dimensional and surface averaged quantities are not required. Second, the poloidal magnetic field is calculated as a triangle function (constant over the area of the triangle), and although  $B_{\chi}$  is zero at the x-point it is always non-zero on the triangles. As a result, all the flow velocities (also triangle functions) are finite. Third, from the metric used in this calculation (Eq. II-18) the quantity  $dx/B_{\chi}$  is just the length (in centimeters) along a flux surface; and thus, the numerical integration required to obtain the electrostatic potential (Eq. II-41) is finite. Simply put, the computational algorithm treats the x-point in the same way as any other point in the system.

Purely classical transport coefficients are used in the calculations presented here. Ideally, neoclassical coefficients should be used, especially in the scrape-off layer but this is not expected to drastically affect the nature of the results. The boundary conditions on the limiter are chosen to be the simplest possible. The density, temperature and poloidal velocity go to zero. Neoclassical coefficients and more realistic boundary conditions on the limiter will be incorporated in any future modifications of the code.

One of the most important questions concerning a discharge that has a separatrix is the role of the separatrix in determining the diffusive flow and, in particular, does the separatrix present any barrier to the flow. Our results indicate that the separatrix does not hamper the diffusive flow across the flux surface. This result is obvious by examining the expression for the flow across a flux surface (Eq. II-50). Rewriting Equation II-50, we have

$$V_{\psi} = \frac{c}{B_{\theta}} \left[ \frac{1}{\sigma_b} \left( \frac{j_{\theta}}{f} + \frac{j_s}{h} \right) - \frac{E_{\theta}}{f} \right],$$

and it is clear that  $V_{\psi}$  is not zero on the separatrix, contrary to results obtained from surface-averaged calculations.<sup>16</sup>

This conclusion is borne out in the numerical results as shown in Figure 15. Here we have plotted the  $V_{\psi}$  vectors for approximately half the triangles just interior to the separatrix. The maximum  $r(z)$  - component of  $V_{\psi}$  is  $6.12 \times 10^2$  cm/sec ( $6.16 \times 10^2$  cm/sec). This is the length of the "unit" vector and all vector lengths are scaled to this "unit" length. The diffusive velocity

across the separatrix is nearly uniform around the major portion of the separatrix except near the null point where it is somewhat larger than the average since  $f$  ( $f = B_\chi/B_\theta$ ) is small there.  $V_\psi$  takes on values between 200 and 700 cm/sec with the larger values near the null point.

The  $\chi$ -component of the diffusion velocity in the scrape-off layer is shown in Figure 16. The magnitude of  $V_\chi$  ranges between  $5 \times 10^3$  cm/sec and  $1 \times 10^5$  cm/sec with the larger values appearing near the null point. Note that the stagnation point is far removed from the limiter. This gives rise to a very long flow path on the outside of the plasma discharge. Also note that the particle flow rate is somewhat larger on the outside of the discharge. This increased flow rate is probably due to the smaller toroidal field on the outside. This result may be somewhat fortuitous physically in that the long flow path on the outside may be compensated for by the larger velocity there. This phenomenon is being investigated further by incorporating a more realistic neutral density profile in the scrape-off layer and more realistic boundary conditions on the limiter.

A measure of divertor efficiency can be made by comparing the diffusive flow across the separatrix to the diffusive flow into the divertor throat. The average velocity across the separatrix is

$$\langle V_\psi \rangle \sim 4 \times 10^2 \text{ cm/sec.}$$

The length of the separatrix is

$$L_s = 3.70 \times 10^2 \text{ cm.}$$



Thus a measure of the diffusive flux across the separatrix can be written as

$$\begin{aligned} D_s &= \langle V_\psi \rangle L_s \\ &\approx 1.5 \times 10^5 \text{ cm}^2/\text{sec}. \end{aligned}$$

The average flow velocity along the scrape-off layer is

$$\langle V_\chi \rangle \approx 5 \times 10^4 \text{ cm/sec},$$

and taking the width of the divertor throat to be

$$W_d \approx 16 \text{ cm},$$

the average flux into the divertor throat is

$$\begin{aligned} D_d &= \langle V_\chi \rangle W_d \\ &\approx 8 \times 10^5 \text{ cm}^2/\text{sec}. \end{aligned}$$

The the divertor is capable of accepting the plasma deposited in the scrape-off layer.

The pressure, density and temperature profiles after several diffusion times are illustrated in Figures 17-19.

## VII. SUMMARY AND CONCLUSIONS

We have developed a fully two-dimensional equilibrium and transport computer simulation model and applied it to the investigation of the poloidal divertor system. The model is unique in that it uses as a finite difference mesh a general connectivity triangular grid. The advantages of this model are numerous.

- 1) Complicated geometries can be handled with a minimum of difficulty.

- 2) The resolution across the mesh is highly variable.

- 3) The Eulerian-Lagrangian nature of the model allows the gross dynamics of the plasma and diffusion and transport to be followed.

- 4) The finite resistivity of the plasma and shell permit the simulation of discharges for times exceeding the field penetration time of the shell.

- 5) The poloidal currents are induced in a self-consistent manner so as to ensure force balance.

- 6) The currents are found in closed form.

- 7) The gradient operator, as a triangle function, is exact.

- 8) In spite of the orders of magnitude difference between the flow along and across the flux surfaces, the conservation equations exactly conserve mass and energy.

- 9) Numerically, there is nothing peculiar about the x-point.

Applying this model to an investigation of the poloidal divertor system we are able to show that physically there is also

nothing peculiar about the x-point; that is, the major portion of the plasma discharge is not affected by the presence of an x-point. The diffusive flow across the separatrix is nearly uniform, around the perimeter of the separatrix. We have found that there is a very long flow path on the outside of the discharge. This may be compensated for somewhat by the increased poloidal velocity in this region. The flux across the separatrix is comparable to the flux into the divertor throat. A conclusion as to whether the divertor can remove impurities effectively and permanently must await modification to the code to include various neutral density profiles and a sheath potential on the limiter.

#### ACKNOWLEDGMENTS

Drs. John L. Johnson and Michio Okabayashi of the Princeton Plasma Physics Laboratory have contributed numerous valuable suggestions to the development of this model. Ufa Christiansen provided magnetic field calculation routines which speeded its development. Conversations with Drs. Martin Fritts and Jay Boris at NRL were especially useful. It is a pleasure to acknowledge other useful discussions with Dale Mead, John Greene, Ray Grimm, Alan Boozer, Steve Jardin, Joan Ogden, Teruyo Tamano, and Abe Kadish. This work was supported by the U.S. Department of Energy under Contract EX-76-A-36-1006.

# APPENDIX

In this section we present the components of the viscous stress tensor in our coordinate system. In the momentum equation we need only the parallel component of the viscous drag but we must include both the parallel and perpendicular components in the ion energy equation.<sup>18</sup>

The parallel viscous drag term has the form<sup>21</sup>

$$\underline{F}_b = 4/3 \eta_b \hat{e}_b \nabla_b^2 v_b \quad (A-1)$$

which can be expressed as

$$\underline{F}_b = 4/3 \eta_b \hat{e}_b \frac{f}{h} B_\chi^2 \frac{\partial}{\partial \chi} \left( \frac{f}{h} \frac{\partial v_b}{\partial \chi} \right) \quad (A-2)$$

where  $\eta_b$  is the parallel viscosity coefficient,<sup>8</sup>

$$\eta_b = 0.96 n_i T_i \tau_i$$

and  $\tau_i$  is the ion collision time.

In the  $\hat{e}_b, \hat{e}_s, \hat{e}_\psi$  basis, the components of the viscous stress tensor are<sup>21</sup>

$$\begin{aligned} \pi_{\psi\psi} &= \eta' (\hat{e}_s \hat{e}_\psi + \hat{e}_\psi \hat{e}_s) : \nabla \underline{v} \\ \pi_{ss} &= -\eta' (\hat{e}_s \hat{e}_\psi + \hat{e}_\psi \hat{e}_s) : \nabla \underline{v} \\ \pi_{\psi s} &= \pi_{s\psi} = \eta' (\hat{e}_\psi \hat{e}_\psi - \hat{e}_s \hat{e}_s) : \nabla \underline{v} \\ \pi_{\psi b} &= \pi_{b\psi} = \eta' (\hat{e}_s \hat{e}_b + \hat{e}_b \hat{e}_s) : \nabla \underline{v} \\ \pi_{sb} &= \pi_{bs} = \eta' (\hat{e}_\psi \hat{e}_b + \hat{e}_b \hat{e}_\psi) : \nabla \underline{v} \end{aligned}$$

where

$$\eta' = \frac{1}{2} \frac{n_i T_i}{\Omega_i} \quad (A-4)$$

the velocity is

$$\underline{v} = v_\psi \hat{e}_\psi + v_b \hat{e}_b + v_s \hat{e}_s$$

and

$$\begin{aligned} \nabla \underline{v} = & \hat{e}_\psi \hat{e}_\psi \left[ \frac{RB}{\chi} \frac{\partial v_\psi}{\partial \psi} + \underline{v} \cdot \nabla \ln \frac{1}{RB} \right] - v_\psi \cdot \nabla \ln \frac{1}{RB} \\ & + \hat{e}_b \hat{e}_b \left[ \frac{fB}{h} \frac{\partial v_b}{\partial \chi} + \underline{v} \cdot \nabla \ln \frac{h}{fB} \right] - v_b \cdot \nabla \ln \frac{h}{fB} \\ & + \hat{e}_s \hat{e}_s \left[ -\frac{B}{h} \frac{\partial v_s}{\partial \chi} + \underline{v} \cdot \nabla \ln \frac{h}{B} \right] - v_s \cdot \nabla \ln \frac{h}{B} \end{aligned} \quad (A-5)$$

Expanding equations A-3, the components of the viscous stress tensor are

$$\begin{aligned} \pi_{\psi\psi} = -\pi_{ss} &= \eta' \left[ v_\psi \frac{B}{h} \frac{\partial}{\partial \chi} \ln \left( \frac{1}{RB} \right) - v_s \frac{RB}{\chi} \frac{\partial}{\partial \psi} \ln \left( \frac{h}{B} \right) \right] \\ \pi_{\psi s} = \pi_{s\psi} &= \eta' \left[ \frac{RB}{\chi} \frac{\partial v_\psi}{\partial \psi} + \frac{B}{h} \frac{\partial v_s}{\partial \chi} + \underline{v} \cdot \left( \Delta \ln \frac{1}{RB} - \Delta \ln \frac{h}{B} \right) \right] \\ \pi_{\psi b} = \pi_{b\psi} &= 2\eta' \left[ v_b \frac{B}{h} \frac{\partial}{\partial \chi} \ln \frac{h}{fB} - v_s \frac{fB}{h} \frac{\partial}{\partial \chi} \ln \frac{h}{B} \right] \\ \pi_{sb} = \pi_{bs} &= -2\eta' \left[ v_b \frac{RB}{\chi} \frac{\partial}{\partial \psi} \ln \frac{h}{RB} + v_\psi \frac{fB}{h} \frac{\partial}{\partial \chi} \ln \frac{1}{RB} \right] \\ \pi_{bb} &= \frac{4}{3} \eta_b \frac{fB}{h} \frac{\partial v_b}{\partial \chi} \end{aligned} \quad (A-6)$$

The total heat generated by the viscosity is given by

$$Q_\eta = \underline{\pi} : \nabla \underline{v} \quad (A-7)$$

Expanding the above, we have

$$\begin{aligned}
 Q_{\eta} = & 4/3 \eta_b \left( \frac{fB}{h} \frac{\partial v_b}{\partial \chi} \right)^2 \\
 & + 2\eta' \frac{RB^2}{h} \left[ RB_{\chi} \frac{\partial v_{\psi}}{\partial \Psi} + \frac{B}{h} \frac{\partial}{\partial \chi} v_s + \underline{v} \cdot \left( \nabla_{\chi} \frac{1}{RB_{\chi}} - \nabla_{\chi} \frac{h}{B_{\chi}} \right) \right] \\
 & \left[ v_{\psi} \frac{\partial}{\partial \chi} \frac{1}{RB_{\chi}} - v_s \frac{\partial}{\partial \Psi} \frac{h}{B_{\chi}} \right] \\
 & - 4\eta' \frac{Rf^2 B^4}{h^3} \left[ v_b \frac{\partial}{\partial \Psi} \frac{h}{RB_{\chi}} + v_{\psi} \frac{\partial}{\partial \chi} \frac{1}{RB_{\chi}} \right] \left[ v_b \frac{\partial}{\partial \chi} \frac{h}{fB_{\chi}} - v_s \frac{\partial}{\partial \chi} \frac{h}{B_{\chi}} \right]
 \end{aligned} \tag{A-8}$$

This expression is quite complicated and an ordering must be imposed to make it more tractable. Physically we know

$$v_{\psi} \ll v_b, v_s.$$

And, in general, the logarithmic derivatives are smaller than the other terms in the expression since they involve "geometric" factors.

We calculate the total viscous stress tensor according to Equation (A-3) but subsequently drop all the logarithmic terms in Equation (A-5) to find an approximate expression for the viscous heating term

$$Q_{\eta} \approx 4/3 \eta_b \left( \frac{fB}{h} \frac{\partial v_b}{\partial \chi} \right)^2 - \eta' \frac{RB^2}{h} v_s \left[ RB_{\chi} \frac{\partial v_{\psi}}{\partial \Psi} + \frac{B}{h} \frac{\partial v_s}{\partial \chi} \right] \left( \frac{\partial}{\partial \Psi} \frac{h}{B_{\chi}} \right) \tag{A-9}$$

This completes the terms we need to include viscosity in our model.

#### REFERENCES

1. G. Laval, et al., Plasma Physics and Controlled Nuclear Fusion Research (Proc. of 7th Int. Conf., Madison 1971) 2, 507 (1971).
2. P. Ohkawa and H. G. Voorhies, Phys. Rev. Lett. 22, 1275 (1969).
3. D. M. Meade, et al., Plasma Physics and Controlled Nuclear Fusion Research (Proc. 5th Int. Conf., Japan 1974).
4. M. Okabayashi and D. Meade, private communication.
5. J. H. Gardner and J. P. Boris, NRL Memorandum Report No. 3152 (Nov. 1975).
6. M. H. Emery, J. H. Gardner, M. Fritts, J. Boris and N. Winsor, NRL Memorandum Report No. 3744 (March 1978).
7. J. P. Boris and K. L. Hain, Bull. Am. Phys. Soc., paper 6G1, p. 942 (October 1974).
8. J. D. Callen and R. A. Dory, Physics of Fluids 15, 1523 (1972).
9. M. D. Kruskal and R. M. Kulsrud, Physics of Fluids 1, 265 (1968).
10. M. H. Emery, J. Gardner, M. Fritts, J. Boris and N. Winsor, Proceedings of the Annual Controlled Fusion Theory Conf., Gatlinberg (1978).
11. S. I. Braginskii, in Reviews of Plasma Physics, ed. by A. Leontovich (Consultants Bureau, New York, (1965), Vol. I, p. 205.
12. D. F. DuChes, D. E. Post and P. H. Rutherford, Nuclear Fusion 17, 565 (1977).



13. N. K. Winsor, Ph.d. Thesis, Princeton University, 1969.
14. Y. Pao, Physics of Fluids 19, 1177 (1976).
15. N. K. Winsor, J. L. Johnson and J. M. Dawson, J. Comp. Phys.  
6, 430 (1970).
16. N. K. Winsor and E. C. Bowers, Proc. of 7th Conf. on the  
Numerical Simulation of Plasmas, Washington- D.C. (1970).
17. A. M. Winslow, J. Comp. Phys. 1, 149 (1966).
18. M. J. Fritts and J. P. Boris, J. Comp. Phys 31, 173 (1979).
19. M. Okabagashi, personal communication.

AMPERE'S LAW  $\longrightarrow j_\chi, j_\theta$

$\vec{B} \times$  (OHM'S LAW)  $\longrightarrow V_\psi, V_S$

$\vec{B} \cdot$  (MOMENTUM EQUATION)  $\longrightarrow V_b$

$\vec{B} \cdot$  (OHM'S LAW)  $\longrightarrow E_\chi, E_\theta, \phi(x, \psi)$

CONTINUITY EQUATION  $\longrightarrow \rho^n$

ENERGY EQUATION  $\longrightarrow T_I^n, T_E^n$

FARADAY'S LAW  $\longrightarrow \Phi^n, \psi^n$

Fig. 1 - Outline of the transport calculation. The first four lines illustrate the calculation of the dynamical variables: the poloidal ( $j_\chi$ ) and toroidal ( $j_\theta$ ) current densities (the perpendicular ( $v_\psi, v_s$ ) and parallel ( $v_b$ ) velocity components; the poloidal ( $E_\chi$ ) and toroidal ( $E_\theta$ ) electric fields and the electrostatic potential ( $\phi(x, \psi)$ ). The last three lines represent the time advance of the mass density ( $\rho^n$ ), the ion ( $T_I^n$ ) and electron ( $T_E^n$ ) temperatures and the toroidal ( $\Phi^n$ ) and poloidal ( $\psi^n$ ) magnetic fluxes.

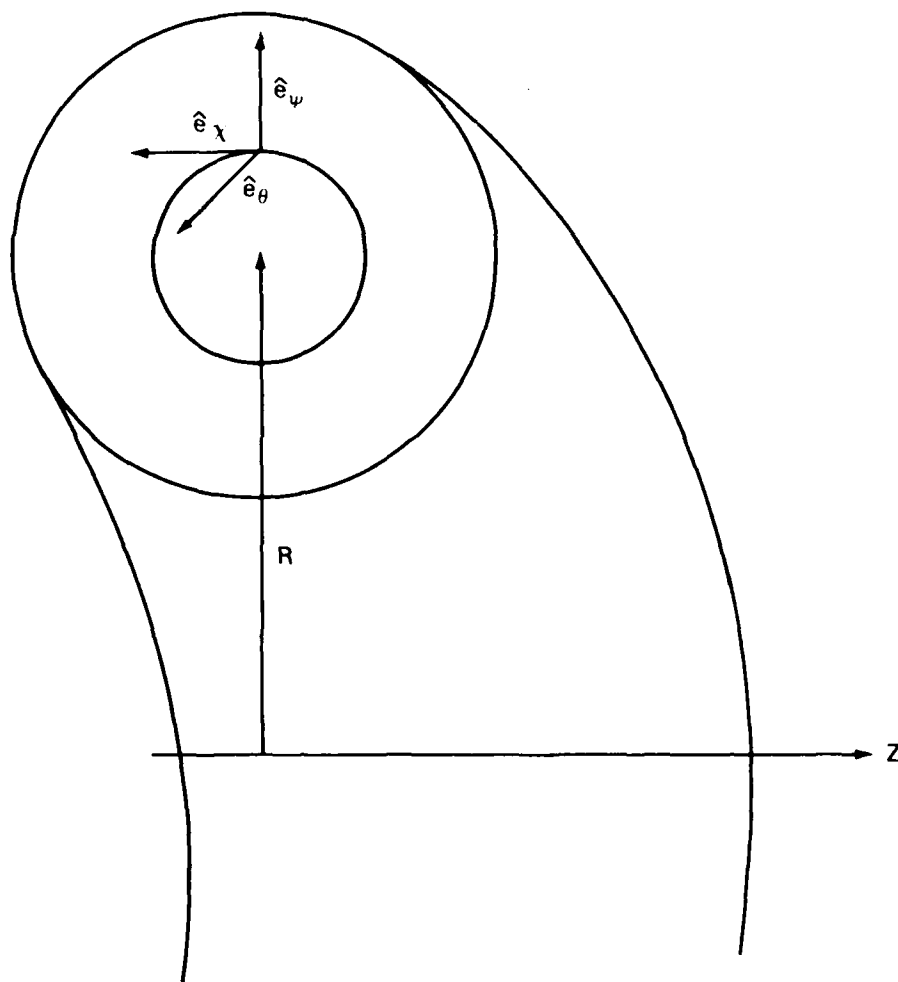


Fig. 2 - The toroidal coordinate system.  $\hat{e}_\chi$  is along the flux surface in the direction of the poloidal magnetic field.  $\hat{e}_\psi$  is perpendicular to the flux surface.  $\hat{e}_\theta$  is in the toroidal (ignorable)  $\psi$  direction. The poloidal field is measured from the outside, and  $(\hat{e}_\psi, \hat{e}_\chi, \hat{e}_\theta)$  form a right-handed coordinate system.

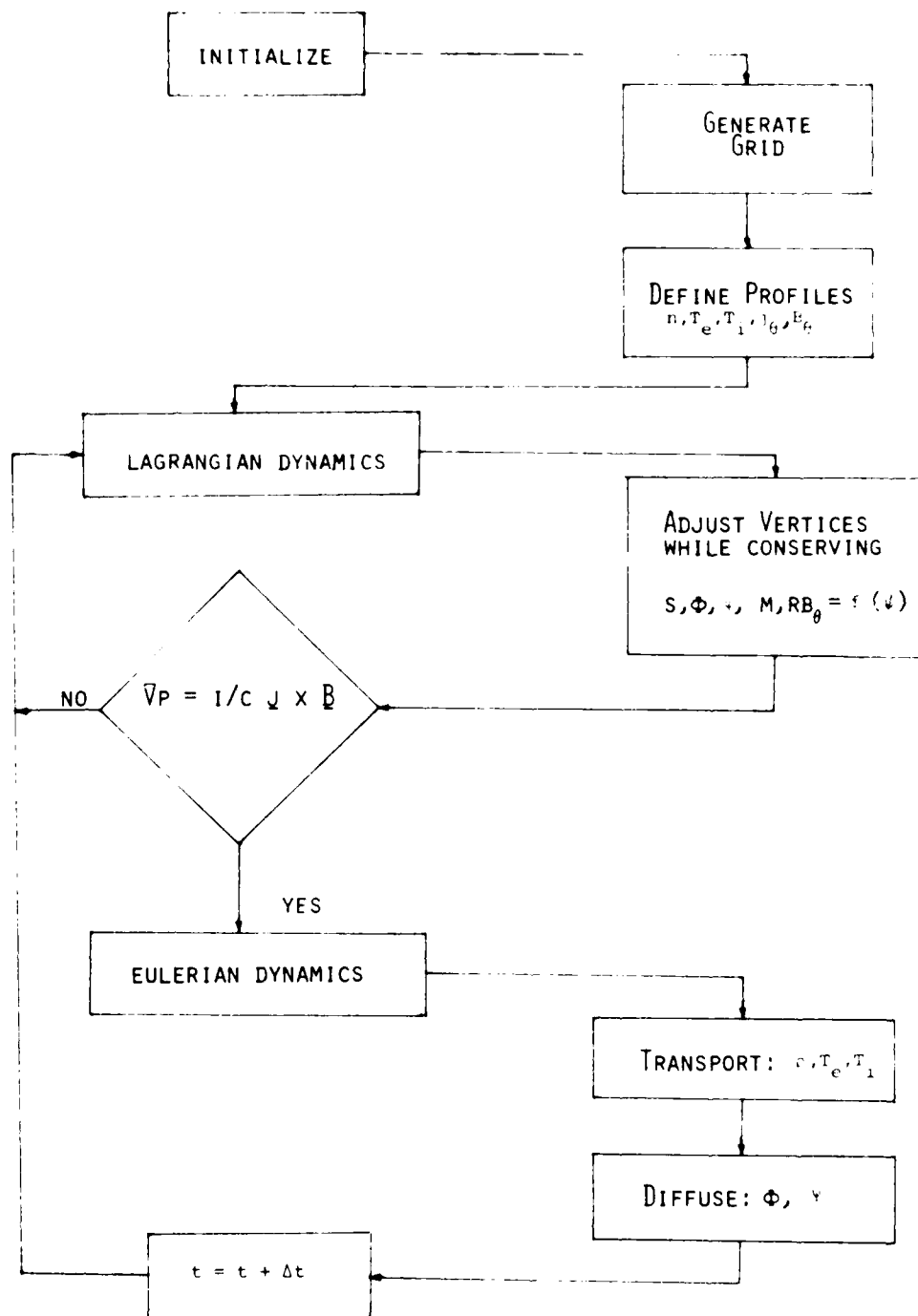


Fig. 3 - Flow chart of complete computational algorithm. The code is split into a Lagrangian part (force-balance) and an Eulerian part (transport). The Lagrangian iteration takes place within the complete timestep loop.

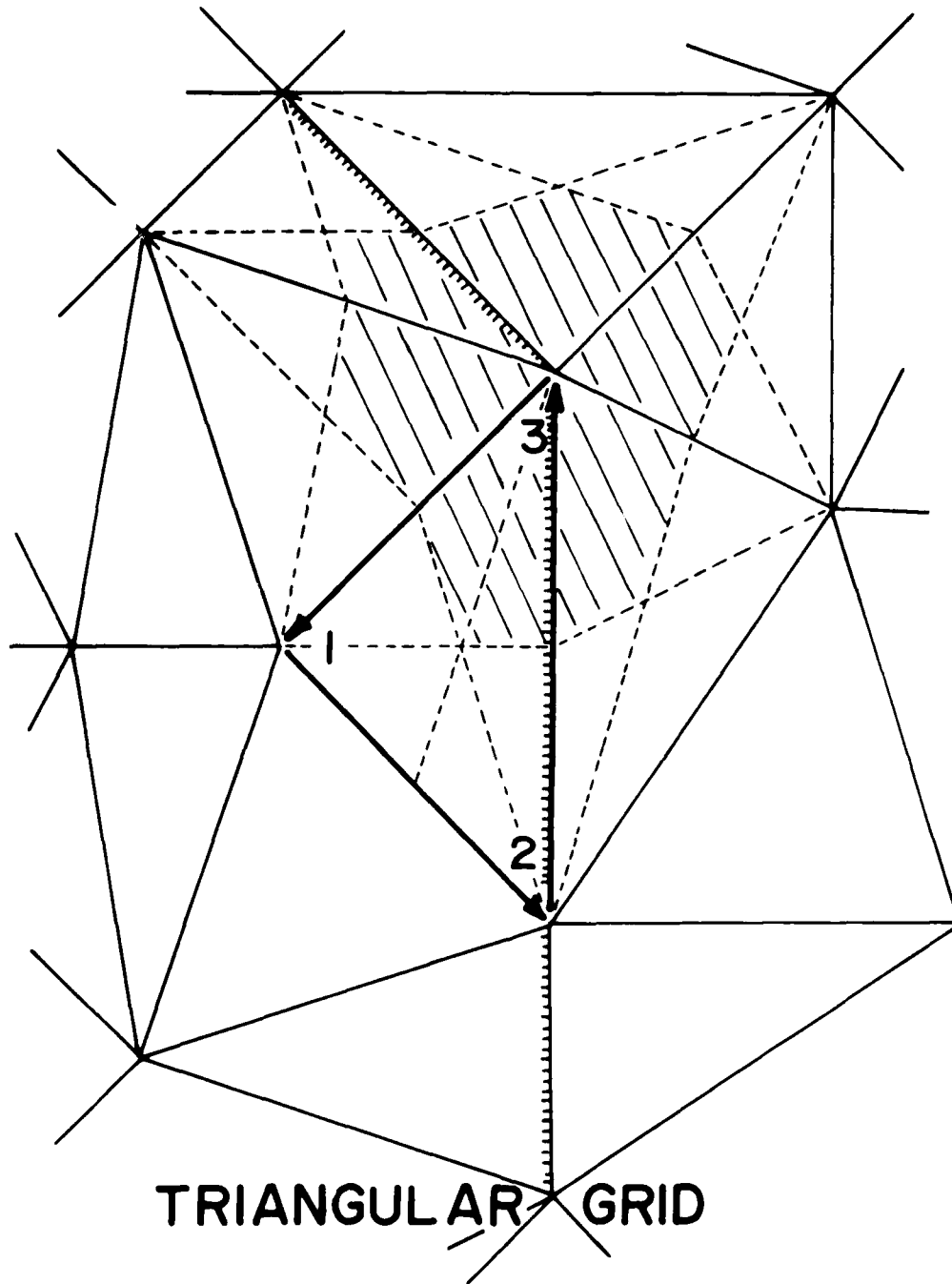


Fig. 4 - Detail of triangular-grid elements. A triangle is made up of three directed line segments, and a vertex represents the (shaded) region defined by the center of mass of each surrounding triangle and the midpoint of each side.

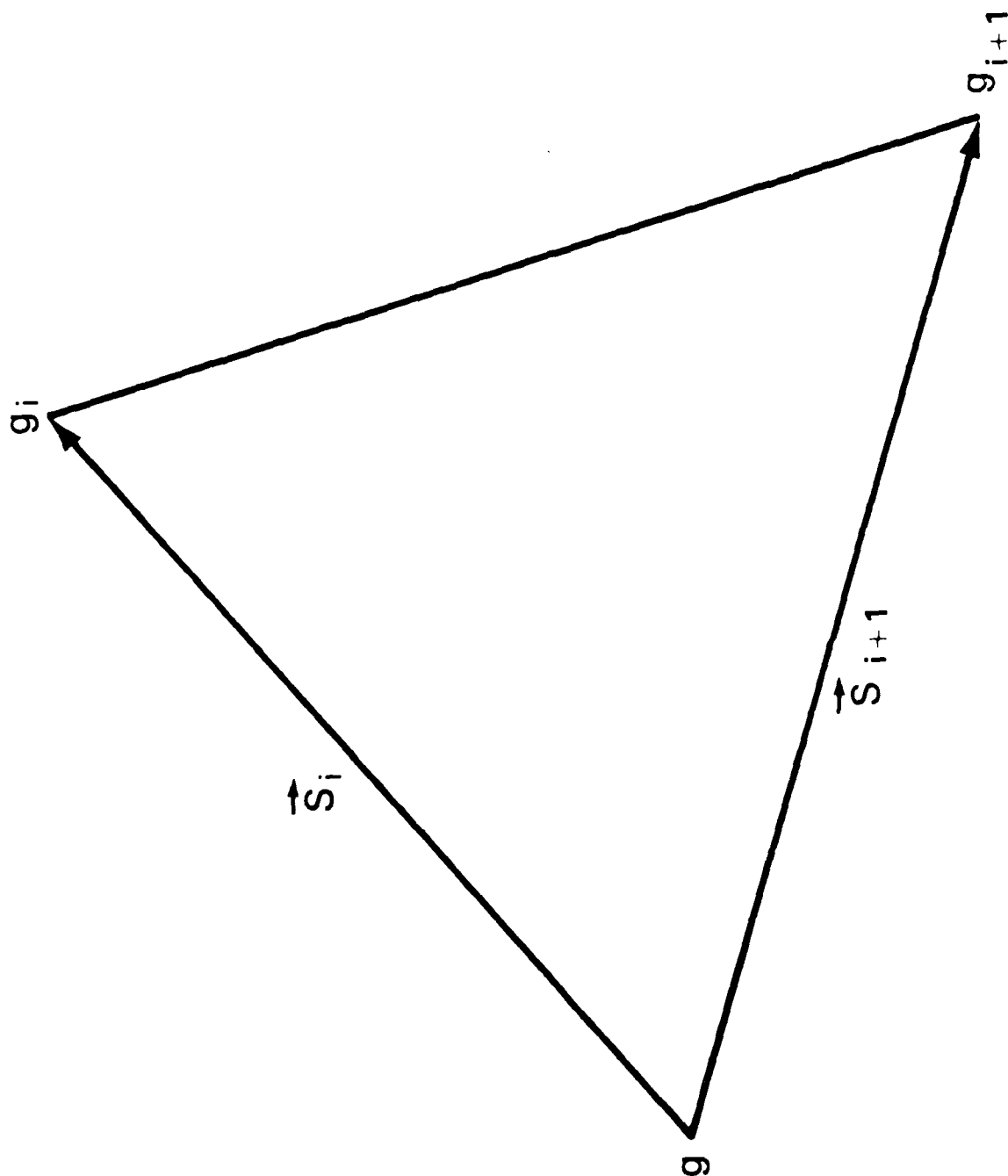


Fig. 5 - The gradient calculation.  $g$  is a vertex function.  $\vec{S}_i$  and  $\vec{S}_{i+1}$  are side vectors which define the triangle.  $g$  is assumed constant over the whole triangle.

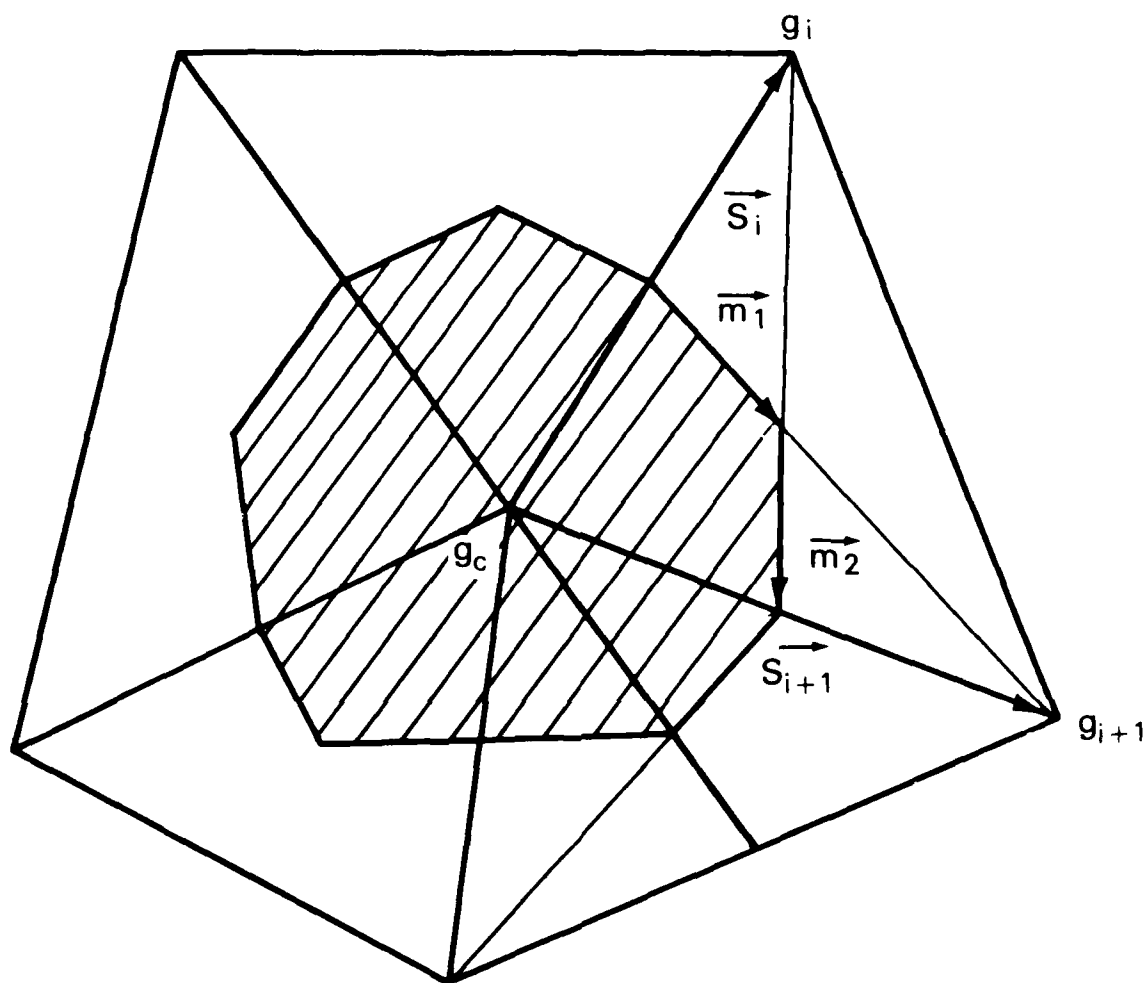


Fig. 6 - Solving the diffusion equation on a triangular mesh. The basic cell function ( $g_c$ ) is integrated forward in time by integrating the triangle functions ( $\lambda \nabla g$ ) around the perimeter of the basic cell.  $\underline{m}_1$  and  $\underline{m}_2$  are the portions of the side bisectors of triangle  $j$  which contribute to the boundary of the basic cell.

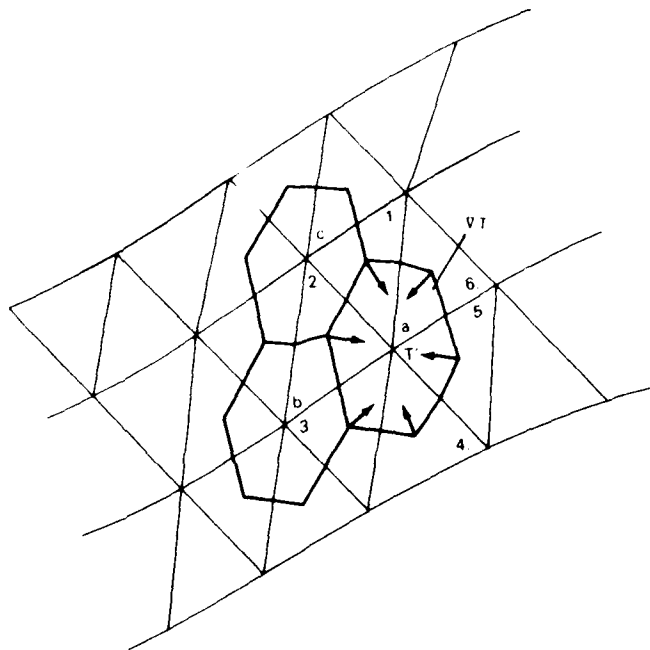


Fig. 7a - Parallel thermal flux calculation. Temperature is assumed non-zero only at vertex  $a$ . The arrows represent  $\Delta T'$ . The parallel thermal fluxes of triangles 1 and 4 are zero. The parallel thermal flux of triangle 2 is normal to the surface of basic cell  $c$ . As a result, no thermal energy is transported across the flux surface.

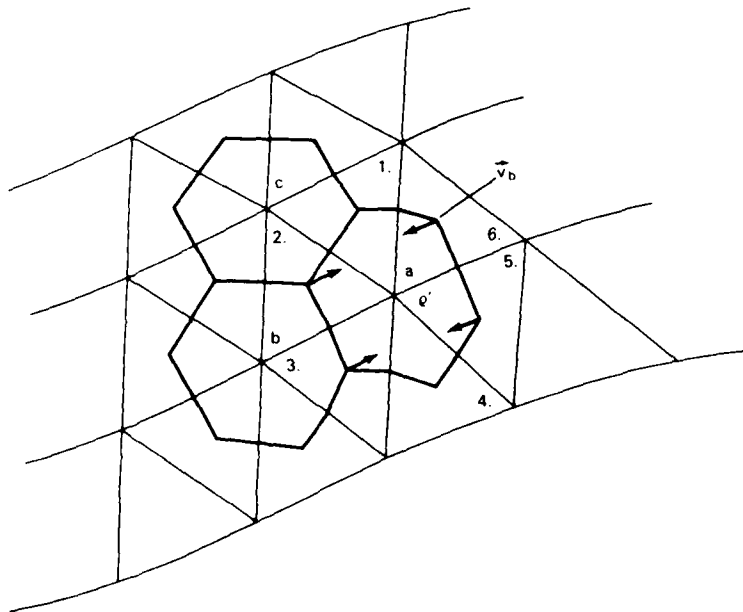


Fig. 7b - Parallel mass flux calculation. The mass density is assumed non-zero only at vertex  $a$ . The parallel velocity is directly proportional to the parallel pressure gradient. The arrows represent  $\underline{v}_b$ . The parallel mass fluxes of triangles 1 and 4 are zero. The parallel mass flux of triangle 2 is normal to the surface of basic cell  $c$ . As a result no mass density is transported across the flux surface.



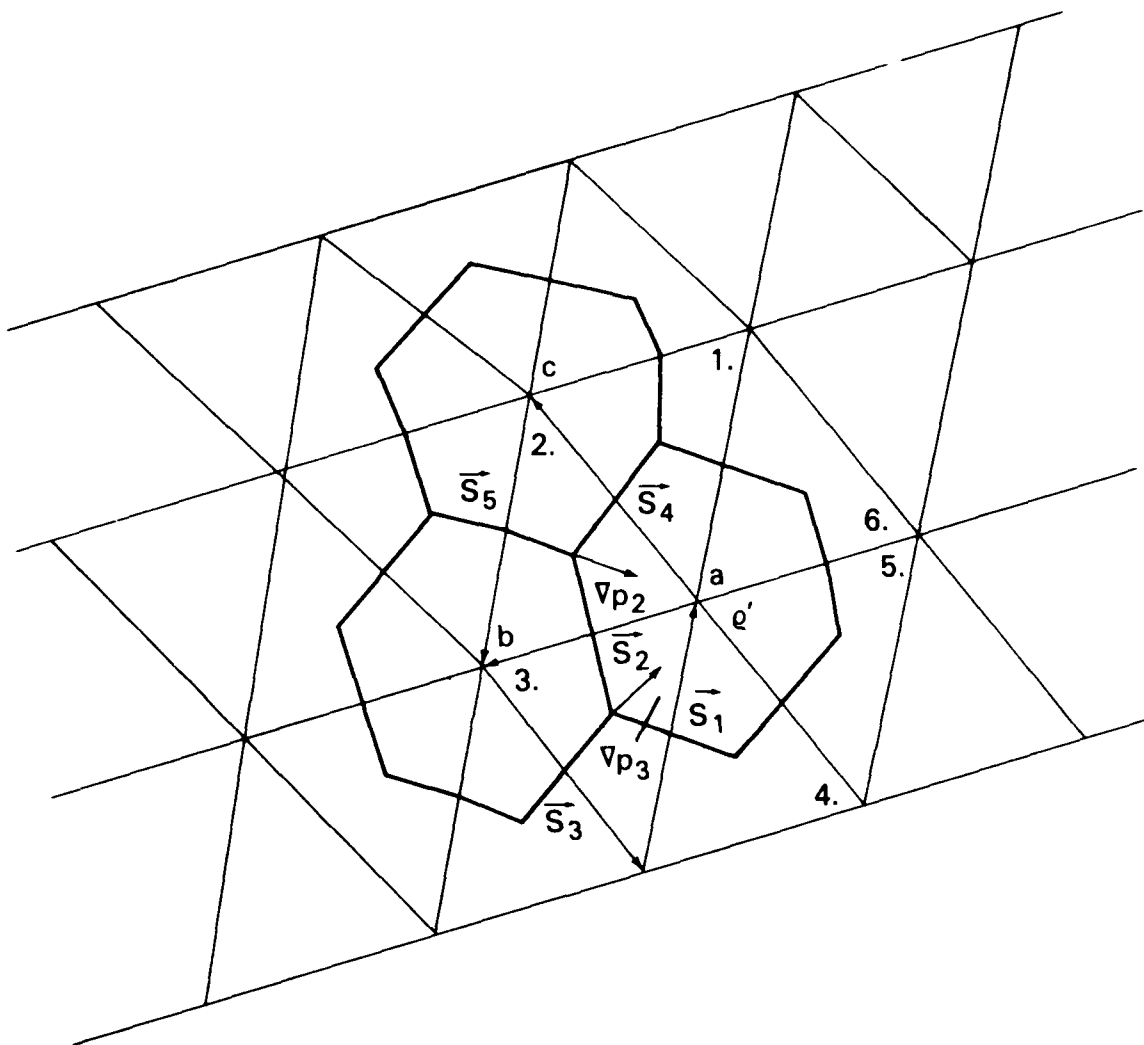
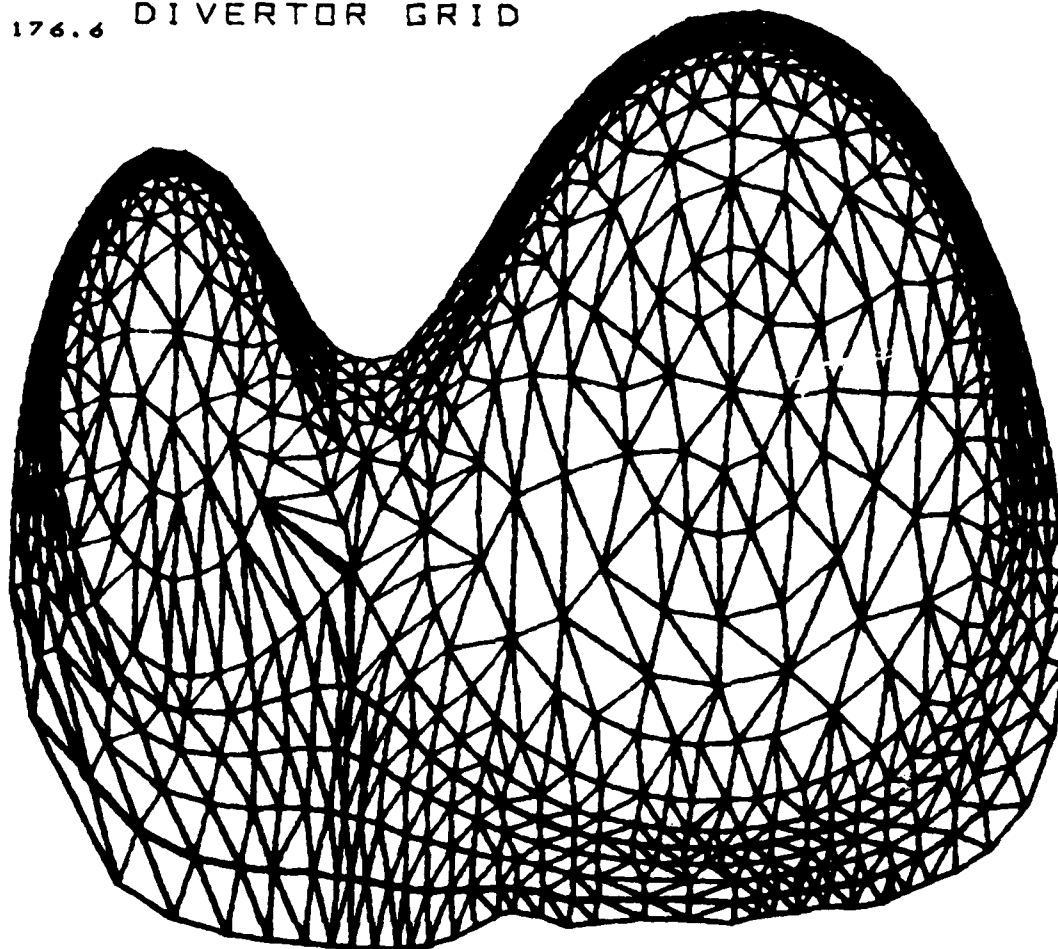


Fig. 8 - Perpendicular mass flux calculation. The mass density is assumed non-zero only at vertex a. For vertex b, the perpendicular flux contribution from triangle 2 is cancelled exactly by the perpendicular flux contribution from triangle 3. As a result, no mass density is transported along the flux surface. Note the counterclockwise direction of the side vectors which define the triangles.

# 176.6 DIVERTOR GRID



45.5  
-141.6

143.7

Fig. 9 - Initial divertor grid configuration. The  $\vec{r}$  direction, pointing away from the axis of symmetry, is "up". The two outermost surfaces make up the copper shell. Moving inward: The next surface is a vacuum surface, the next two surfaces comprise the scrape-off layer, the next surface is the separatrix. The other surfaces make up the divertor, on the left, and the plasma discharge, on the right. Note the high resolution in the scrape-off layer.

# DIVERTOR GRID

176.6

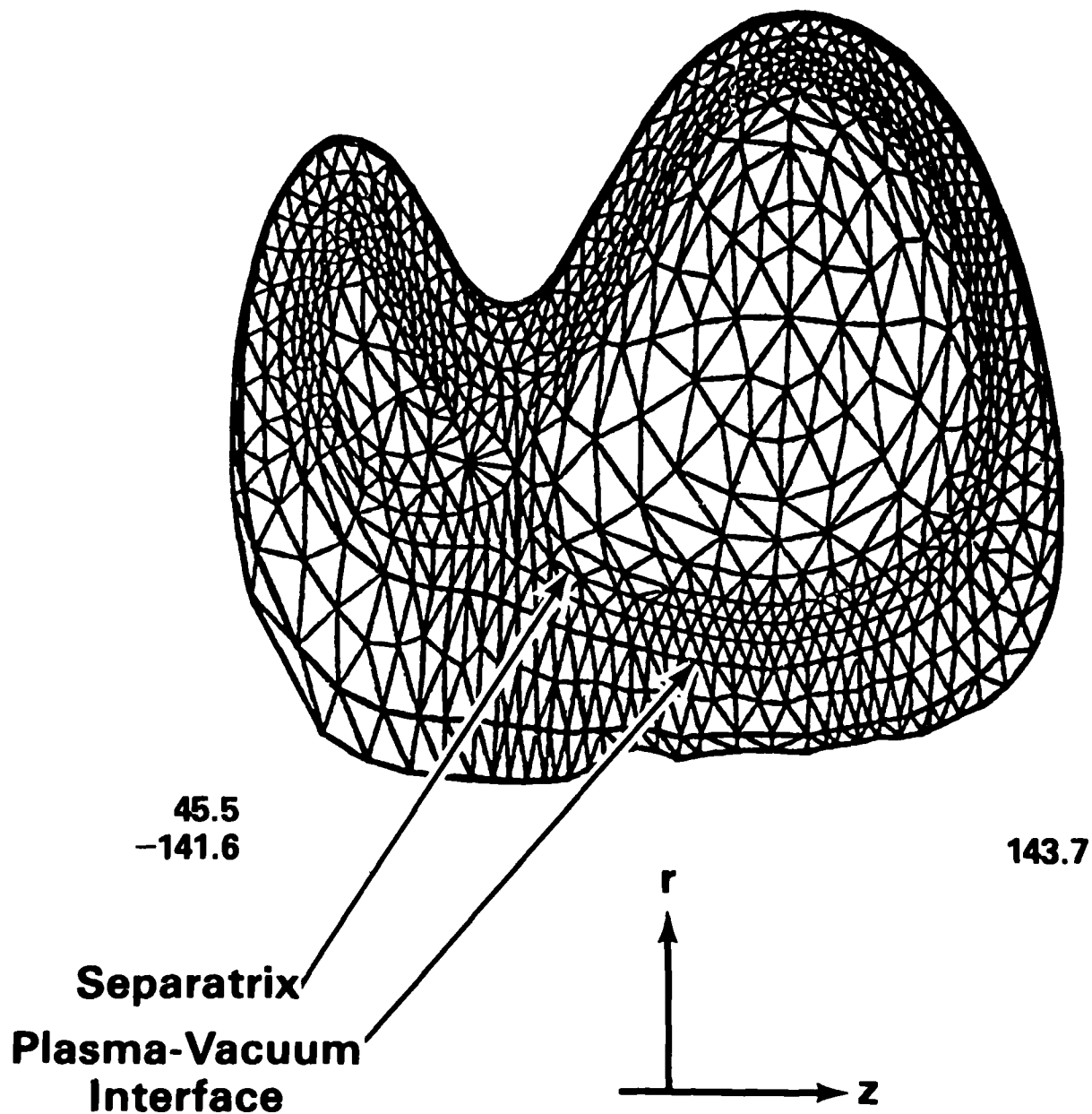


Fig. 10 - Equilibrium grid configuration. The outer surfaces have moved away from the wall giving a clearer picture of the grid structure. Note that the null point is well defined.

# PRESSURE

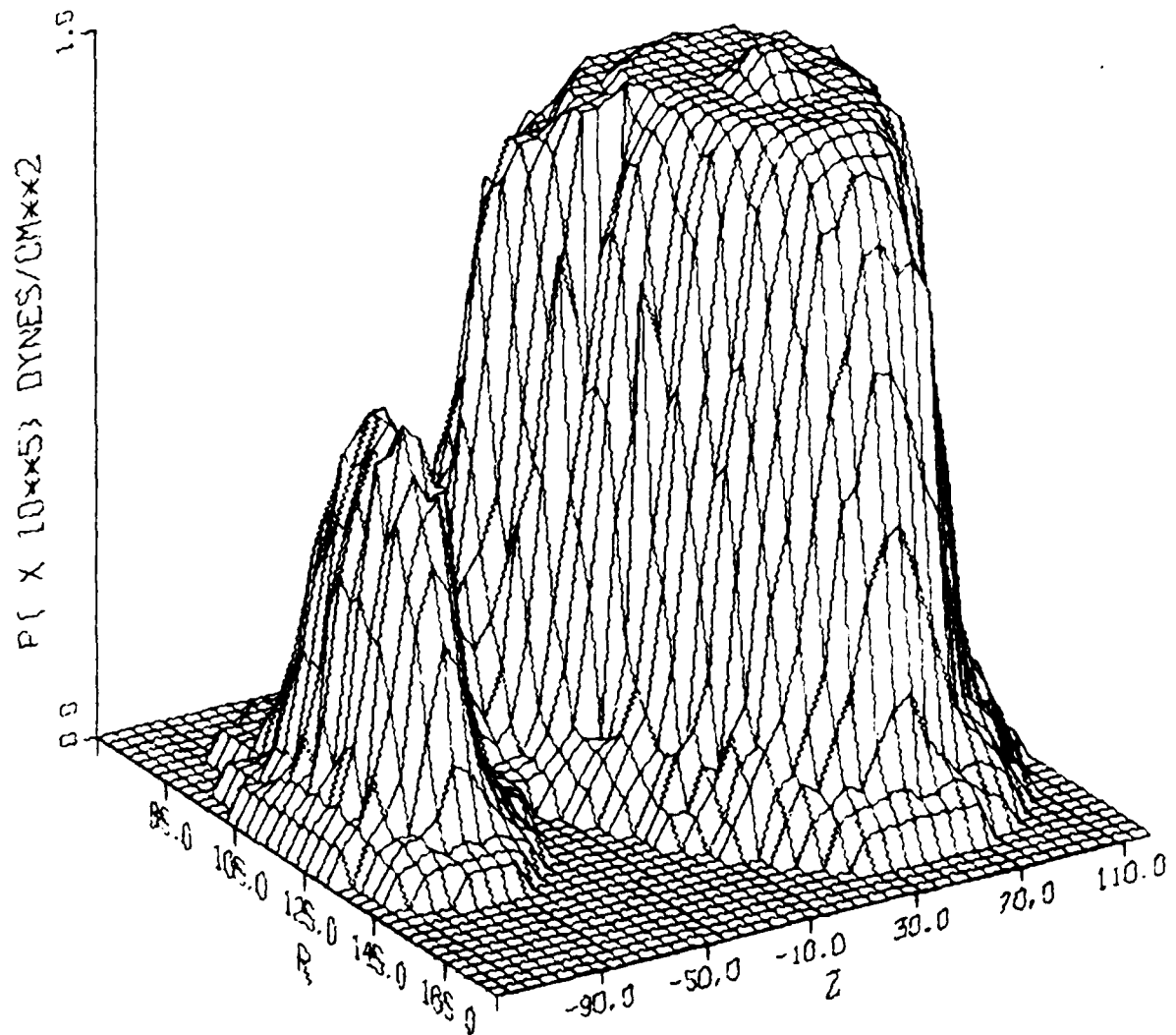


Fig. 11 - Pressure profile. A two-dimensional perspective plot of the pressure. The point of view is from the outside of the discharge; i.e., large  $r$ , looking into the divertor. The  $r$ ,  $z$  dimensions are in centimeters.

# DENSITY

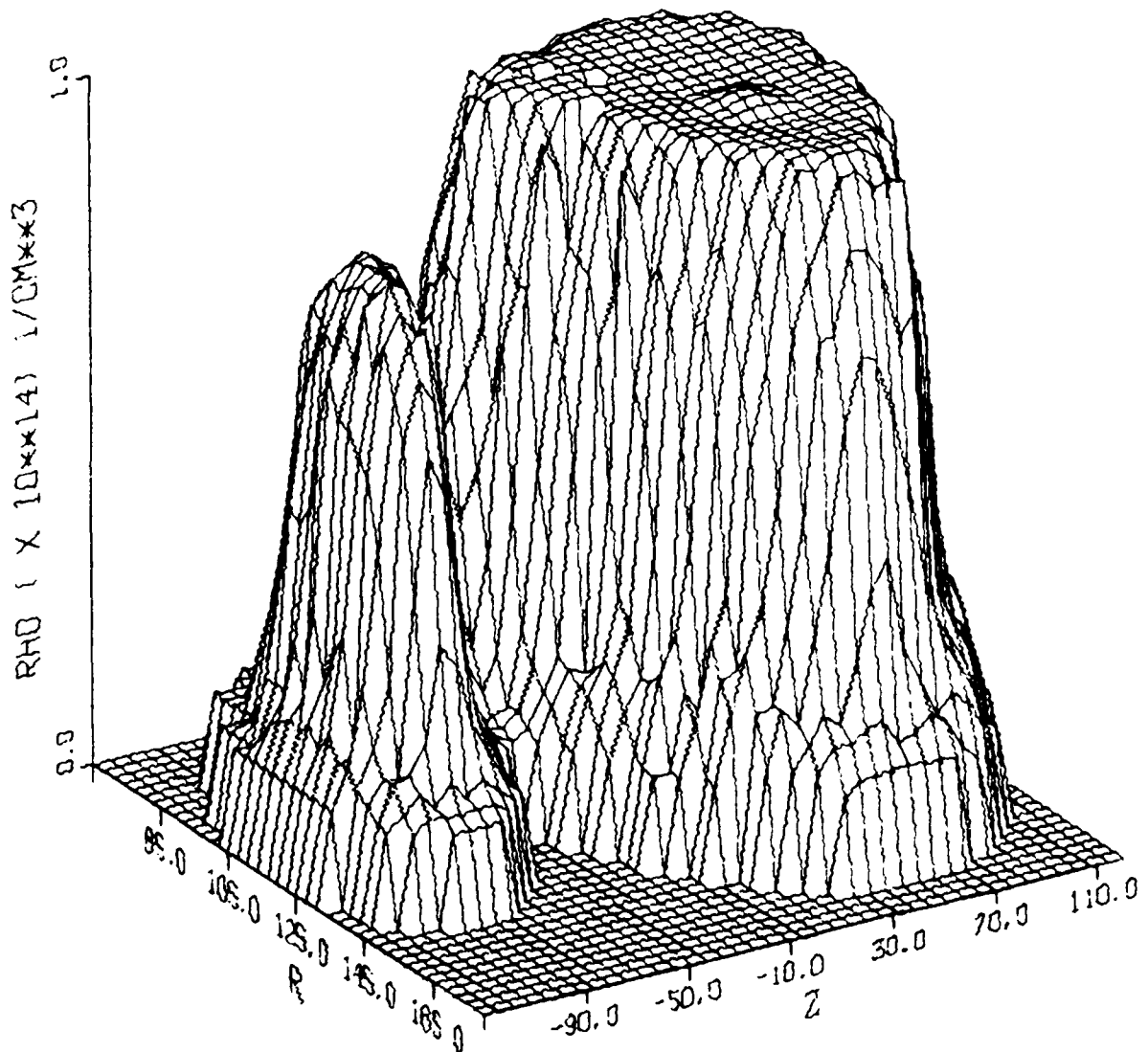


Fig. 12 - Density profile

# TEMPERATURE

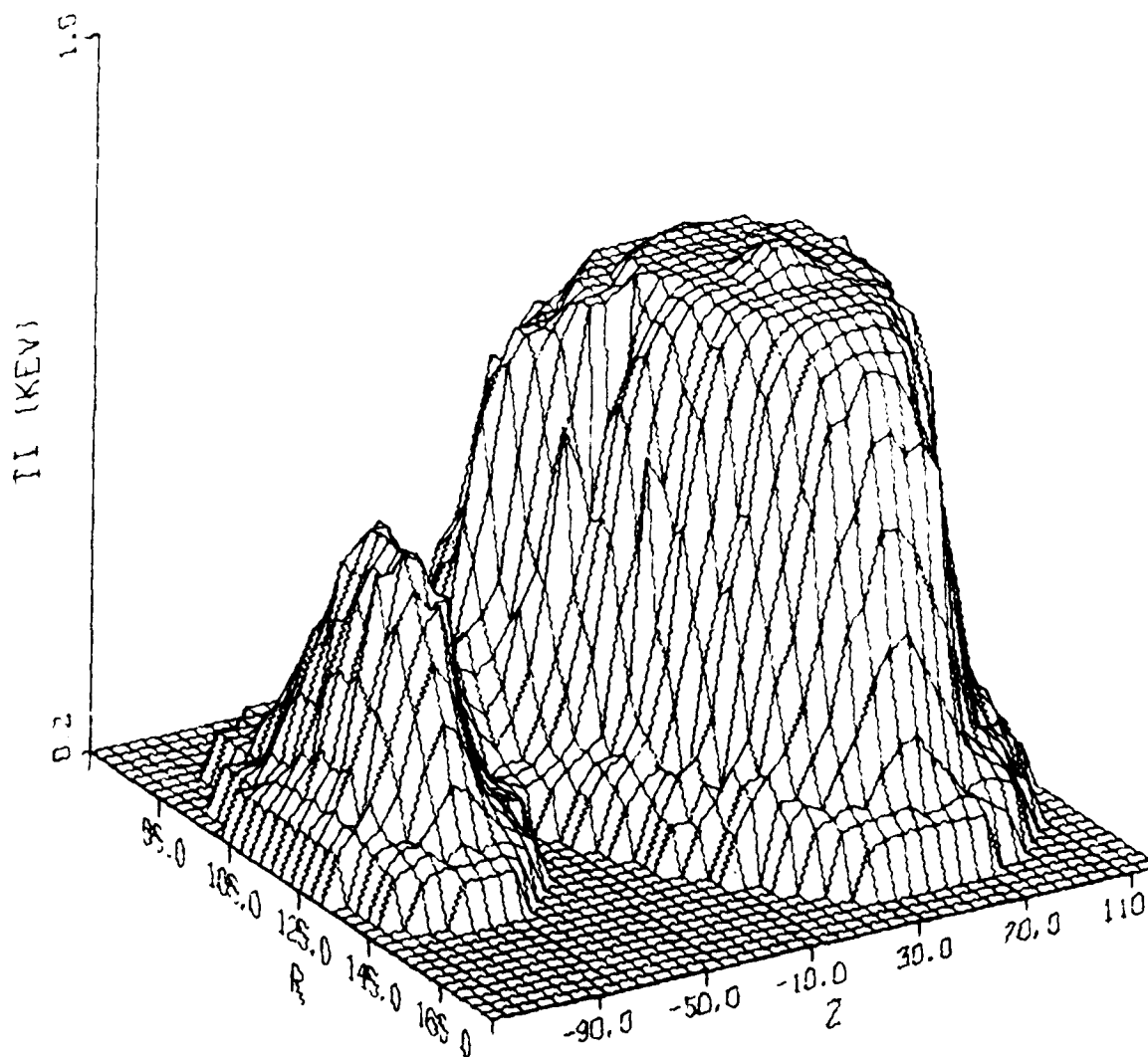


Fig. 13 - Ion temperature profile. The ion temperature is equal to the electron temperature at equilibrium.

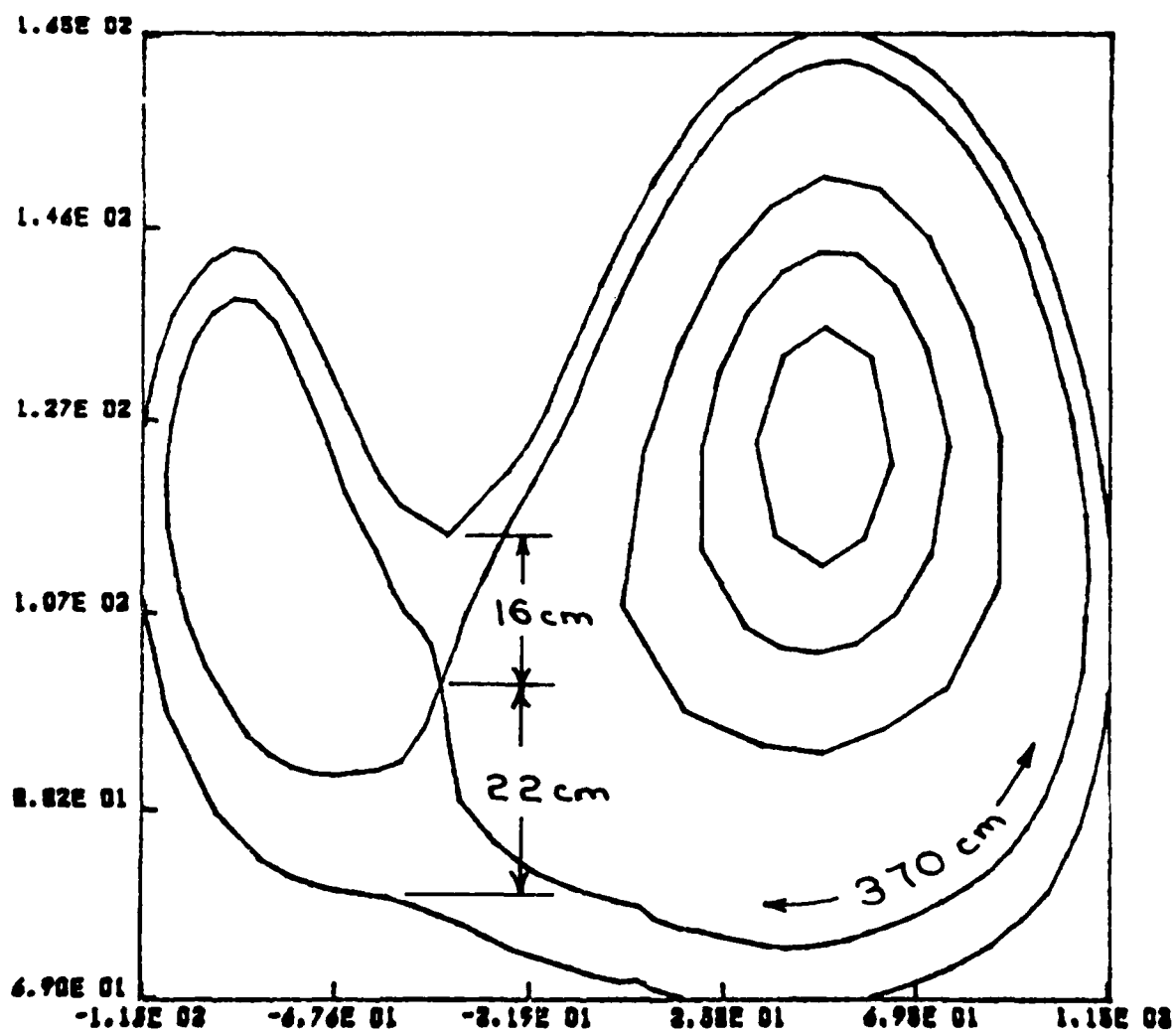


Fig. 14 - Separatrix dimensions. A plot of the separatrix and outer-most plasma surface. The scrape-off layer is 16cm wide on the outside and 22cm. on the inside. The perimeter of the separatrix is 370cm.

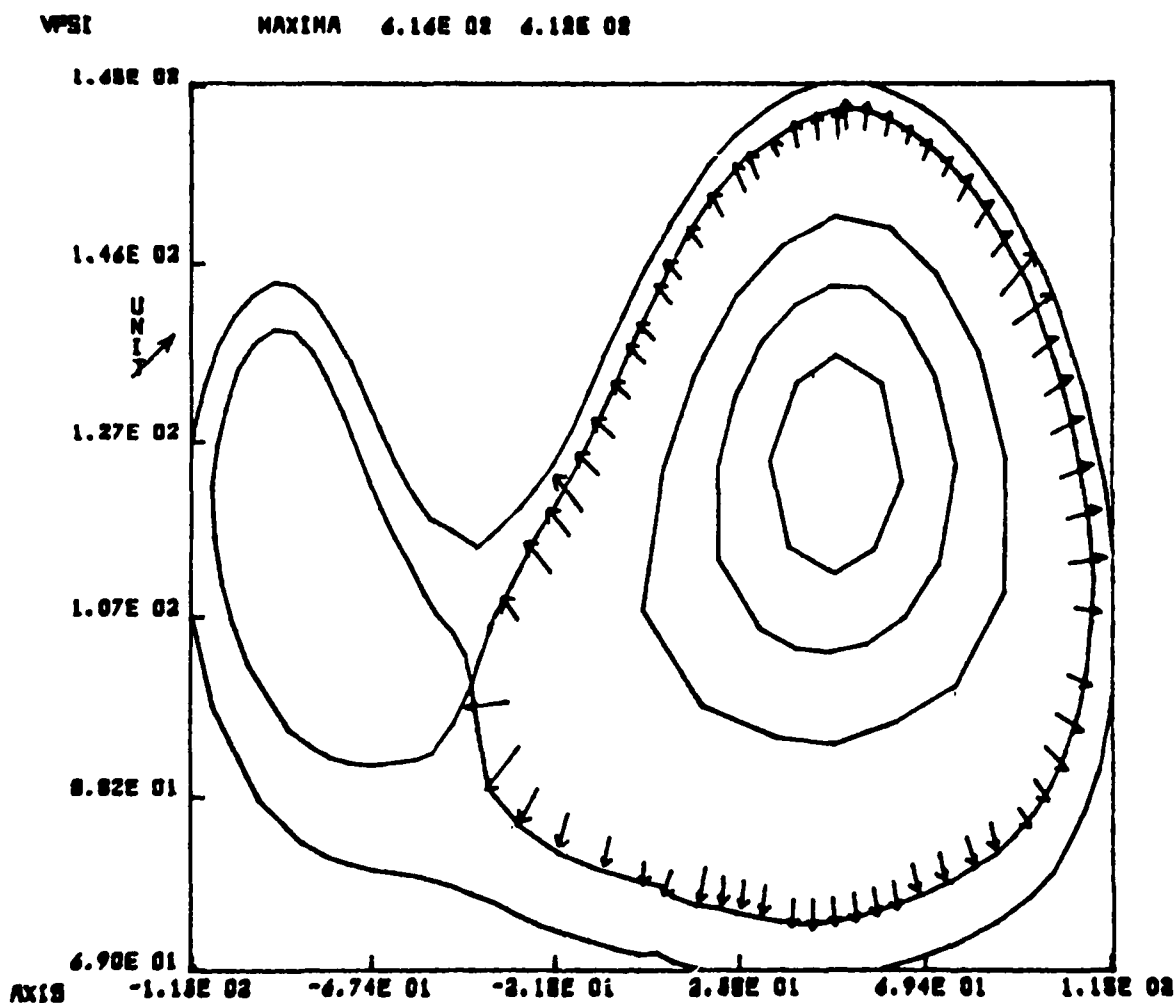


Fig. 15 - Perpendicular flow. The vectors represent the  $\psi$ -component of the diffusive velocity across the separatrix. The vector lengths are scaled to the unit length which has components ( $V_R = 6.12 \times 10^2$  cm/sec,  $V_z = 6.16 \times 10^2$  cm/sec).



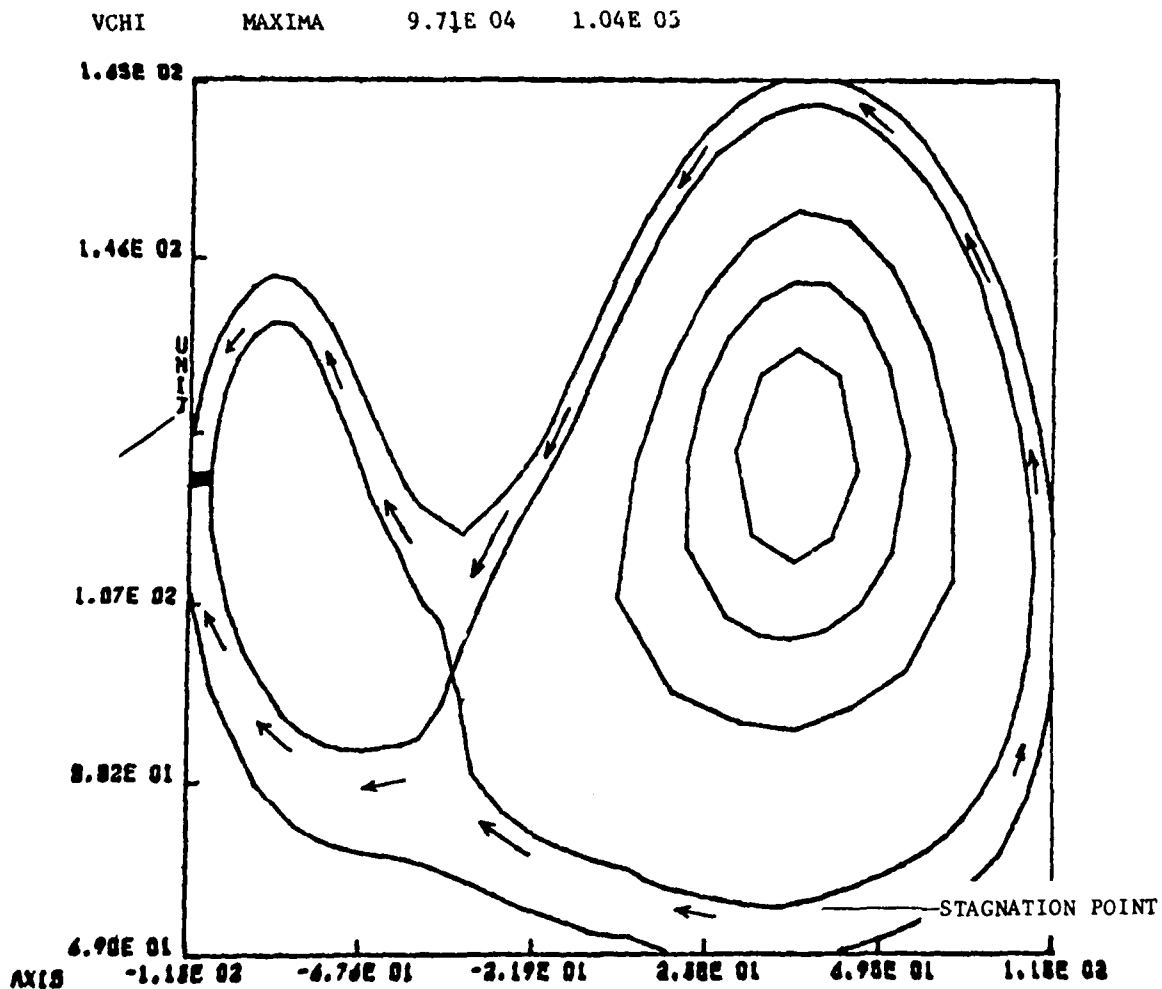


Fig. 16 - Parallel flow. The vectors represent the  $x$ -component of the diffusive velocity in the scrape-off layer. The vector lengths are scaled to the unit length which has components ( $V_R = 9.71 \times 10^4$  cm/sec,  $V_z = 1.04 \times 10^5$  cm/sec). The stagnation region is far from the limiter giving rise to a very long flow path on the outside of discharge.

# PRESSURE

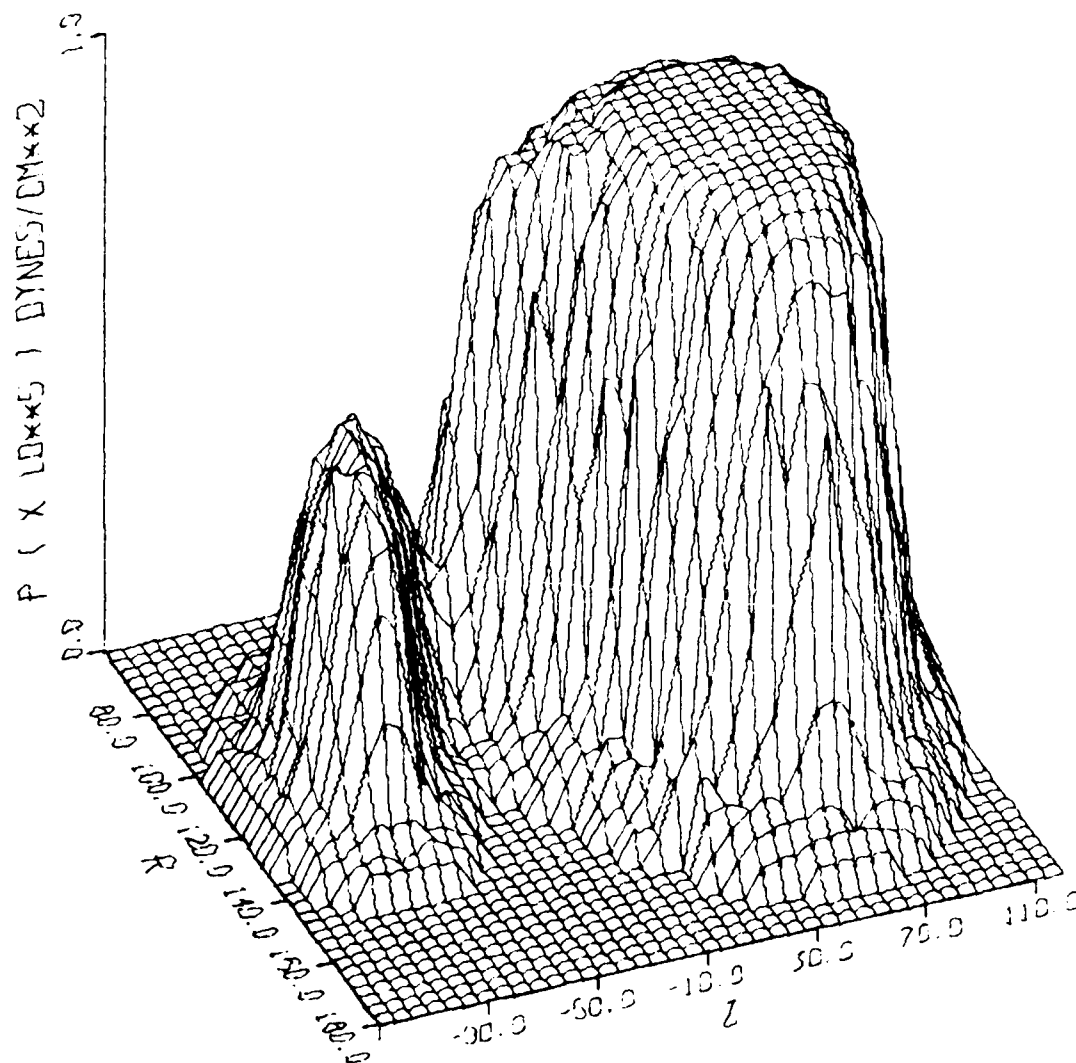


Fig. 17 - Pressure profile. A two-dimensional perspective plot of the pressure after several diffusion times. Note the somewhat flatter profile across the main body of the discharge.

# DENSITY

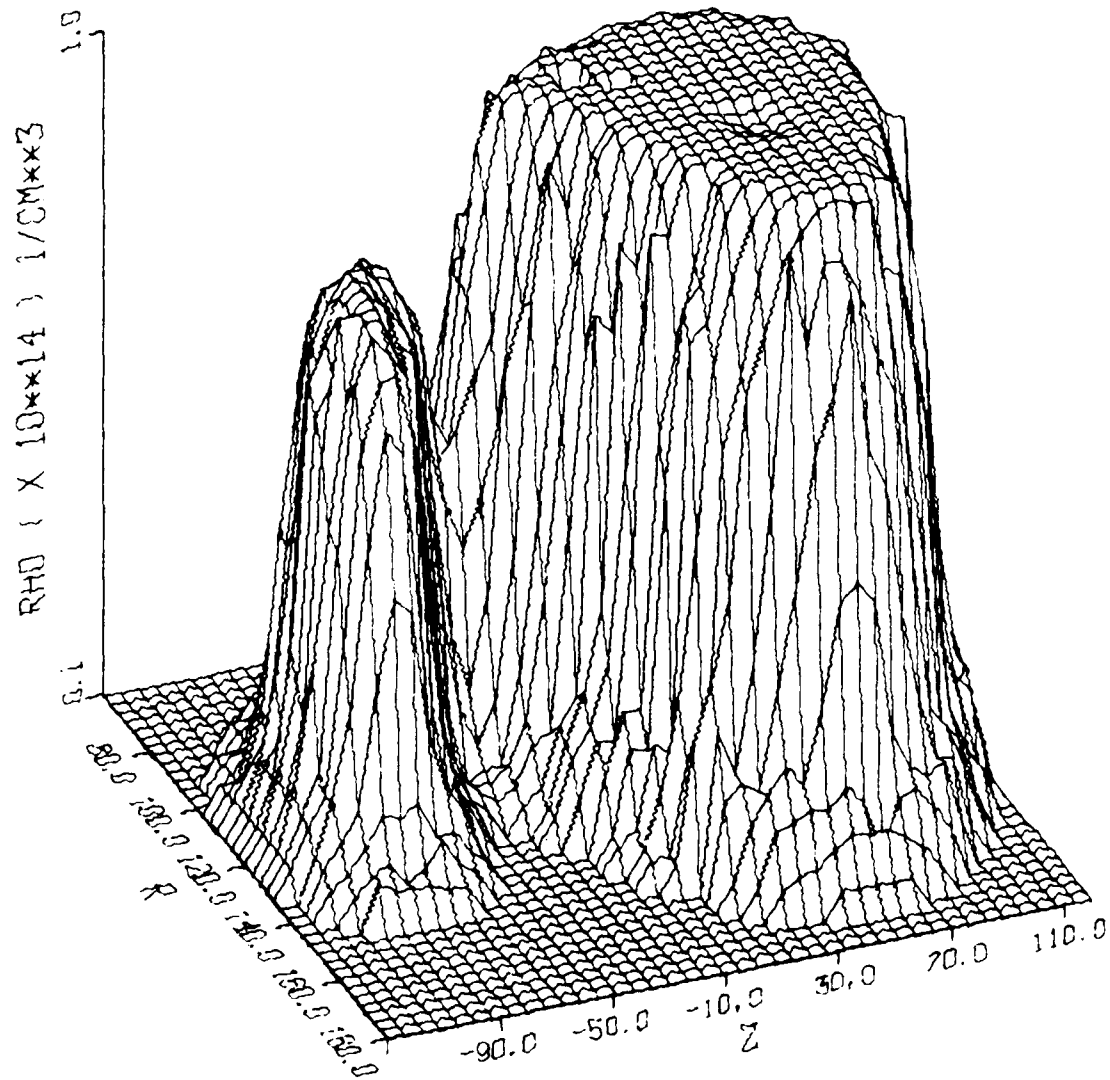


Fig. 18 - Density profile

# TEMPERATURE

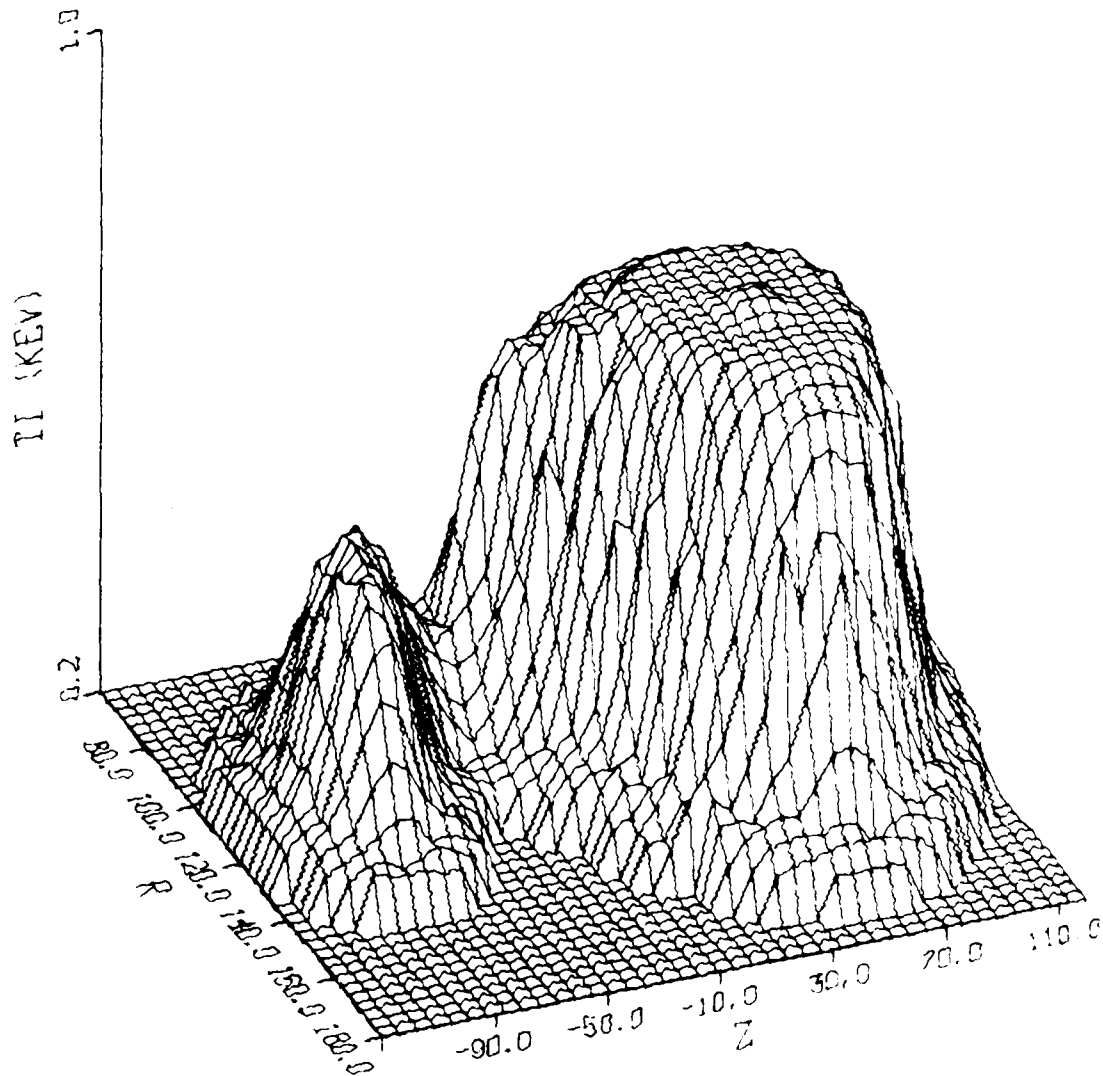


Fig. 19 - Ion temperature profile

# PRESSURE

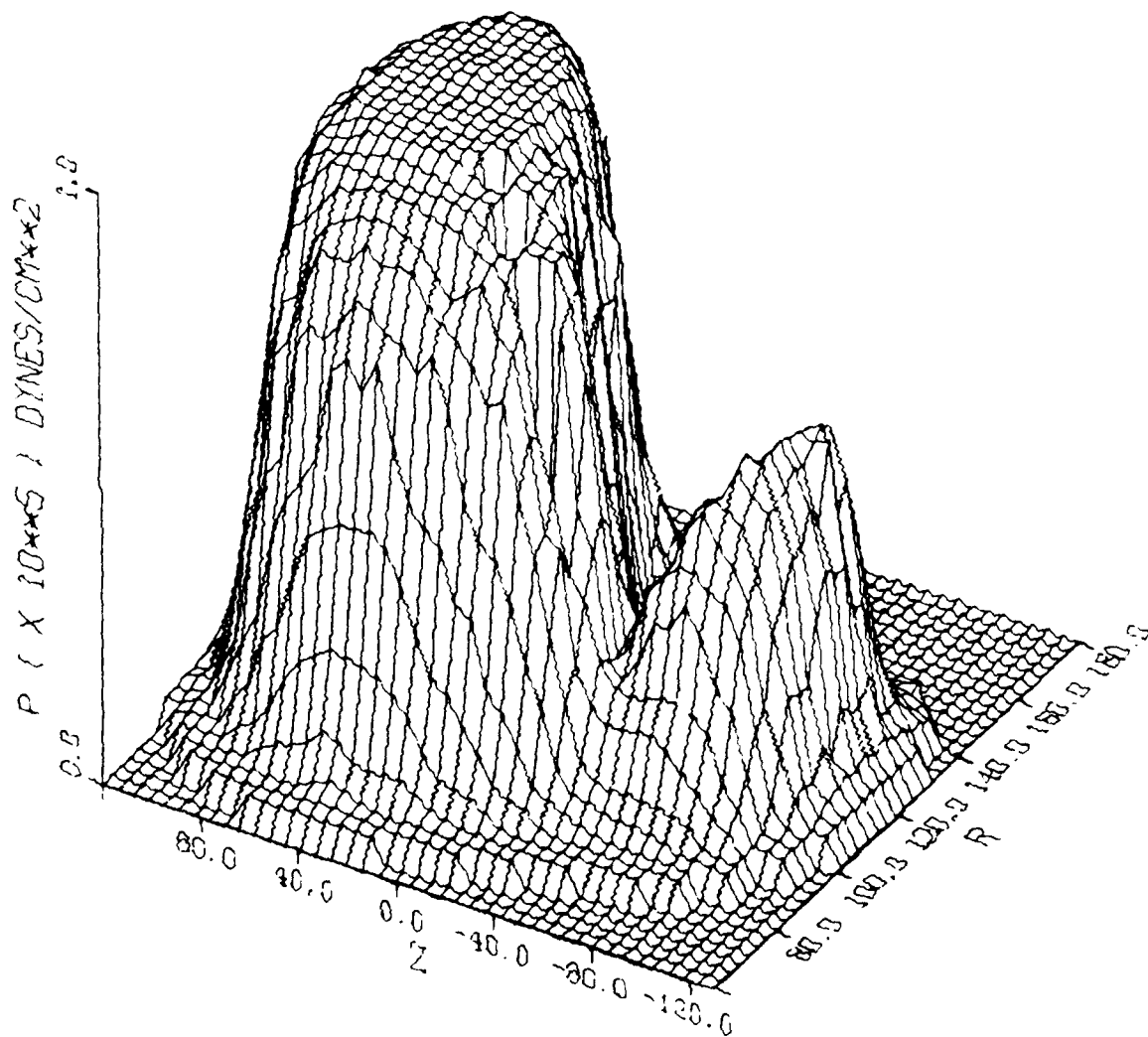


Fig. 20 - Pressure profile. A two-dimensional perspective plot of the pressure as viewed from the inside of the discharge, i.e. small  $r$ .

# DENSITY

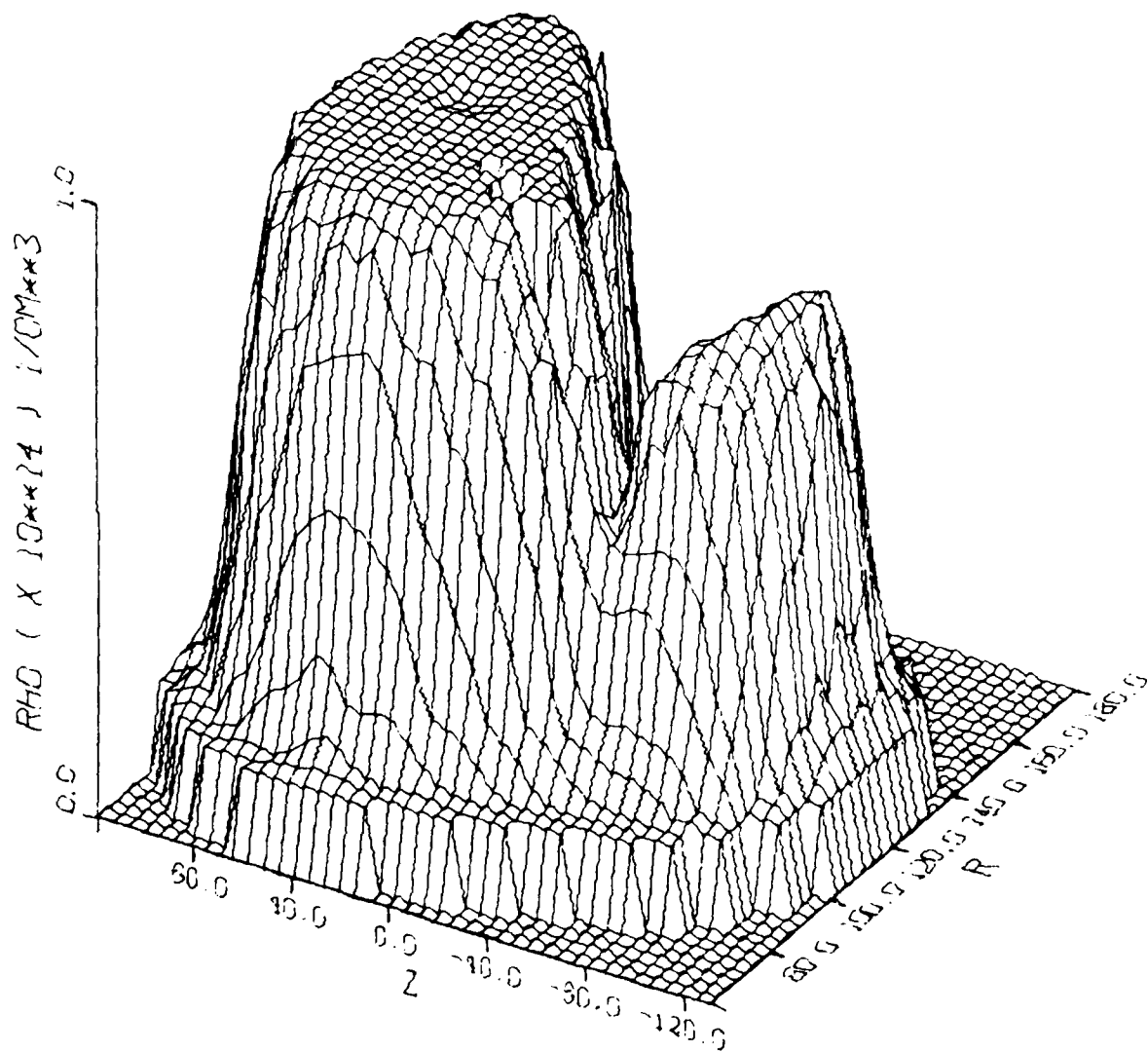


Fig. 21 - Density profile. Same view as Figure 20

# TEMPERATURE

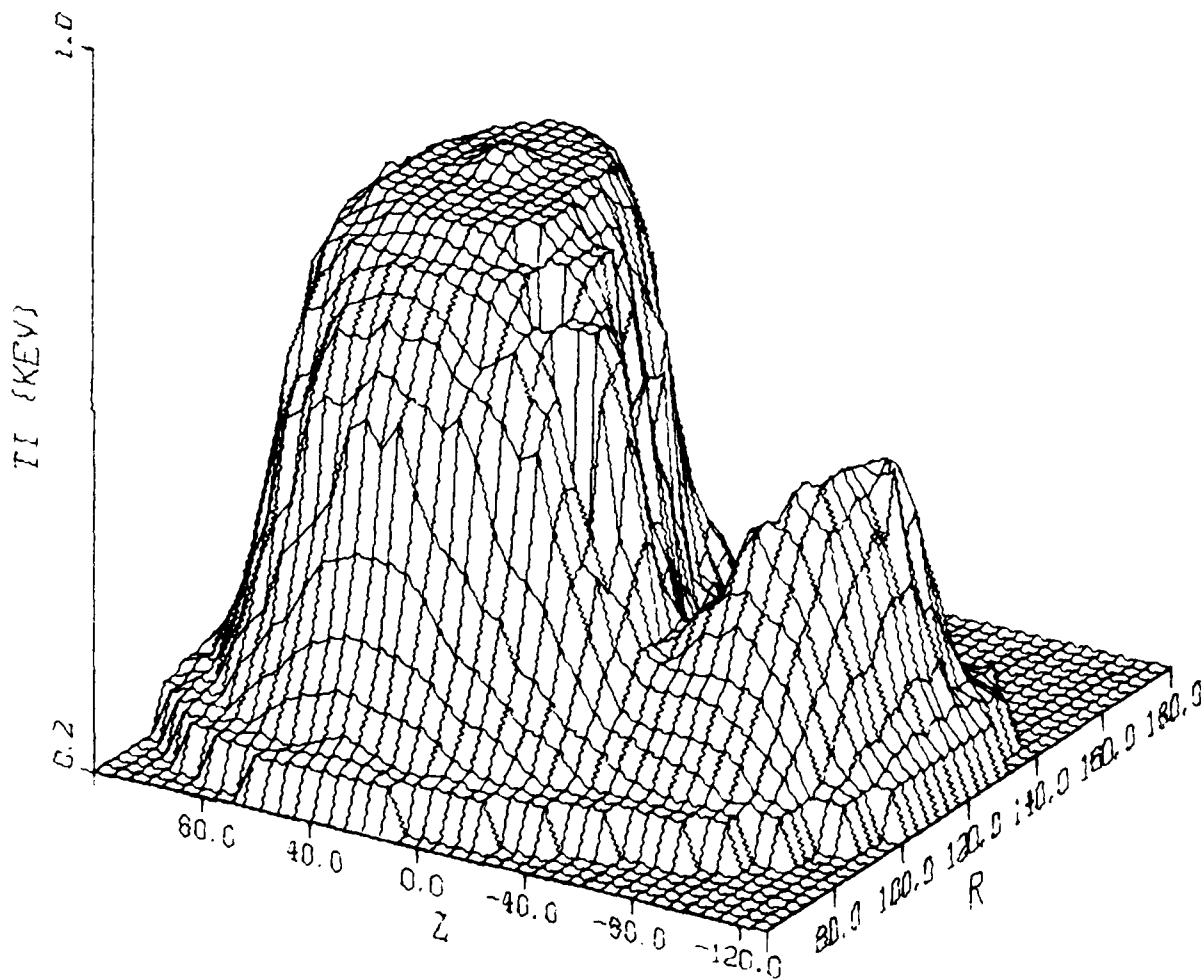


Fig. 22 - Ion temperature profile. Same view as Figure 20.

DISTRIBUTION LIST

DOE  
P.O. Box 62  
Oak Ridge, Tenn. 37830

UC20 Basic List (116 copies)  
UC20f (192 copies)  
UC20g (176 copies)

NAVAL RESEARCH LABORATORY  
Washington, D. C. 20375

Code 4700 (25 copies)  
Code 4790 (150 copies)  
D.Spicer, Code 4169

DEFENSE TECHNICAL INFORMATION CENTER  
Cameron Station  
5010 Duke Street  
Alexandria, VA 22314 (12 copies)



